# Chromosome decompaction and cohesin direct Topoisomerase II activity to establish and maintain an unentangled interphase genome

Erica M. Hildebrand[1], Kirill Polovnikov[2], Bastiaan Dekker[1], Yu Liu[1], Denis L. Lafontaine[1], A. Nicole Fox[1,3], Ying Li[1], Sergey V. Venev[1], Leonid Mirny[4], Job Dekker[1,3,*]

**AFFILIATIONS:**

1. Department of Systems Biology, UMass Chan Medical School, Worcester, MA, 01605

2. Interdisciplinary Scientific Center Poncelet (CNRS UMI 2615), Moscow, Russia

3. Howard Hughes Medical Institute, Chevy Chase, MD, 20815

4. Institute for Medical Engineering and Science, and Department of Physics, Massachusetts Institute of Technology, Cambridge, MA 02139

* Corresponding author

**SUMMARY:**

The topological state of chromosomes is an important factor controlling their mechanical properties, dynamics and function. Recent work has shown that interphase chromosomes are largely free of entanglements. How cycling cells establish this state from a dense mitotic chromosome and maintain it through interphase in the presence of Topoisomerase II activity remains mysterious. Using multi-contact 3C, Hi-C, and polymer simulations, we find that mitotic chromosomes are intrachromosomally entangled, while interphase chromosomes are not, pointing to cell cycle-dependent control of chromosome topology. The majority of mitotic entanglements are removed during anaphase/telophase, with most of the remaining ones removed during early G1, in a process that requires Topoisomerase II. Polymer simulations show that swelling and decondensation of mitotic chromosomes during mitotic exit produce entropic forces that bias Topoisomerase II activity towards decatenation of condensin loops. This is followed by prevention of formation of new entanglements by lower Topoisomerase II activity in G1, and, in heterochromatic B compartments, by interplay between cohesin and Topoisomerase II. Our results show how cells control chromosome topology during mitotic exit and G1 employing both biophysical and molecular mechanisms to modulate Topoisomerase II activity and directionality.

**KEYWORDS:**

Topoisomerase II, Compartment, Heterochromatin, Euchromatin, Genome Architecture, Chromosome Folding, Chromosome Entanglement, Self-Catenation, Mitosis, G1, Cohesin, Fractal Globule, Genome Topology

**INTRODUCTION:**

Topoisomerase II (Topo II) controls the topological state of the genome [1] throughout the cell cycle. This enzyme allows DNA duplexes to pass through one another by catalyzing controlled double strand breaks [1]. There are two forms of Topo II in the human genome, DNA Topoisomerase 2-alpha and DNA Topoisomerase 2-beta, encoded by the *TOP2A* and *TOP2B* genes, respectively [1-9]. TOP2A has well studied roles in organizing mitotic chromosomes where it is both a structural component and is required for decatenation of sister chromatids at anaphase [4,5,10-20]. TOP2B is expressed throughout the cell cycle and its activity has been detected at open chromatin sites and active chromatin including promoters and CTCF sites during interphase [1,21-25]

Whether and how the topological state of chromosomes changes during the cell cycle is not well understood. Hi-C has been widely used to characterize chromosome folding in mitosis and interphase [26], however since Hi-C measures pairwise interactions, one aspect of chromosome folding that is not detected by this method is the entanglement or catenation state of the genome. For the purposes of this study, we define a chromosome entanglement to be a local interlink between two regions of the genome, on the same or different chromosomes. A special type of entanglement operating on rings (loops) is a catenation; catenations can turn a ring into a knotted state or can link two rings (e.g., two chromosome loops). A catenane can also knot a linear chromosome, or a pair of chromosomes, if its ends are sufficiently far away from each other as to behave like a polymer ring. Strand passage facilitated by Topo II can both

remove and create entanglements, catenating or decatenating loops. Previously studies showed that highly entangled chains become highly “intermingled”, allowing indirect inference of the entanglement state from the experimentally measurable level of intermingling, e.g., using multi-contact 3C (MC-3C) [27].

MC-3C and super-resolution chromosome tracing data have shown that interphase chromosomes are largely free of intra-chromosomal entanglements [27,28]. Hi-C data also suggest folding of interphase chromosomes into an unentangled polymer state known as the fractal (crumpled) globule [26]. In contrast, the topological state of mitotic chromosomes is less understood. Self-entanglement is supported by in vitro experiments and some polymer models, with others supporting an unentangled state [29-32]. In their seminal paper A. Rosa and R. Everaers (2008) propose that the unentangled and territorial interphase state is formed by decompaction from an unentangled mitotic chromosome if Topo II is inactive during exit from mitosis [31]. Although assumed absence of Topo II activity during interphase has been challenged by experiments, the Rosa-Everaers model highlights the importance of topological constraints in establishing and maintaining unentangled and territorial chromosomes[31].

We have determined the role of Topo II in chromosome folding transitions during mitotic exit and G1 entry when chromosomes undergo dramatic changes in their folding. We uncover cell cycle stage – dependent differences in chromosome entanglement, and identify the roles of chromosome loops and chromosome decondensation in directing

Topo II activity towards disentanglement rather than entanglement of chromosomes during mitotic exit and interphase.

## RESULTS:

### Topo II inhibition does not affect steady state chromosome folding in interphase

Topo II has roles in formation and maintenance of mitotic chromosome structure, as well as in unlinking of sister chromatids [12,13,33]. In contrast, the relevance of Topo II for decondensation of individual chromatids after their separation and upon G1 entry is less established. Treatment with the bisdioxopiperazine derivative ICRF-193, a potent catalytic inhibitor of both TOP2A and TOP2B, which specifically blocks Topo II enzymes that are engaged with DNA in the process of strand passage by stabilizing a closed clamp conformation [34-36], during G1 entry has previously been shown to cause morphological changes in chromosomes by microscopy [37-42]. However, partial genetic depletion of Topo II during mitosis and G1 entry does not cause major changes in chromosome folding by genomics methods [43]. Here we investigated the genome-wide effect of chemical inhibition of Topo II on chromosome folding and topology genome-wide using Hi-C and MC-3C.

We first determined whether Topo II activity is required for maintenance of G1 chromosome folding. We performed Hi-C 2.0 (Hi-C) on G1 sorted HeLa S3 cells from an asynchronously growing population (AS) after a two-hour treatment with either DMSO or 30uM ICRF-193 [44]. 30uM ICRF-93 is a sufficient dose to block Topo II activity as it completely prevents sister chromatid decatenation during anaphase and stabilizes

Cyclin B when added during release from a mitotic arrest (see methods, [38,45,46]) (Figure 1A,B, Figure S1A-D). Hi-C interaction maps revealed no obvious effect of Topo II inhibition: compartments are detected at similar strength in both conditions, and TADs and loops are unchanged (Figure 1C, K, L, Figure S1J-P, and see below). We conclude that the interphase conformation can be maintained in the presence of Topo II inhibition.

**Topo II inhibition delays compartment re-establishment at G1 entry**

To determine whether Topo II activity is required for establishment of G1 chromosome folding, we performed Hi-C on G1 sorted cells from synchronized HeLa S3 cultures during G1 entry (Figure 1 E, F, Figure S1H-I) [44,47,48]. Cells were first arrested in prometaphase using a single thymidine block + 12 hour nocodazole arrest (*t* = 0), and then synchronously released into G1 with either DMSO or 30uM ICRF-193 added at two hours post nocodazole wash-out (*t* = 2 hrs, when at least 50% of cells have entered or passed anaphase (Figure S1F), and aliquots were fixed for Hi-C using 1% formaldehyde in early G1 (*t* = 4 hrs) or late G1 (*t* = 8 hrs), and G1 cells were isolated using FACS (Figure 1E, Figure S1A, B, E-G, I) [47,48].

In Hi-C data obtained from the Control (DMSO treated) cells, the checkerboard pattern representing compartmentalization is apparent in early G1, but becomes stronger in late G1, as previously reported (Figure 1G) [47,49]. In cells treated with ICRF-193 we observed two phenomena: First, at *t* = 4 hrs, we observe a very weak checkerboard and a broad diagonal of enriched interactions reminiscent of Hi-C data from mitotic chromosomes (Figure 1G, Figure S2G, O) [46,47,50]. Second, at *t* = 8 hrs a nearly normal

compartmentalization pattern is observed, indicating that compartments can be established but with delayed kinetics (Figure 1G).

We can quantify the effect of ICRF-193 in the following ways. First, the ratio of Hi-C interactions detected with ICRF-193 vs. DMSO treated cells at *t* = 4 hrs shows enriched interactions close to the diagonal between A and B domains (Figure 1H). Such a pattern of enriched interactions is reminiscent of what is observed in mitosis (Figure S2G, O) [46,47,50]. By *t* = 8 hrs, this difference is much smaller. Second, analysis of the relationship of interaction frequency (*P*) of pairs of loci as a function of the genomic distance (*s*) between them shows relatively frequent interactions in early G1 with ICRF-193 treatment for loci separated by 2-20Mb compared to interactions detected in untreated cells (Figure 1 I, J, Figure S1K, L). By late G1 (*t* = 8 hrs) *P(s)* curves are comparable with or without ICRF-193 treatment. Finally, we quantified compartment strength at different distances. In ICRF-193 treated cells, A-A and B-B compartment strength is weaker in early G1 (*t* = 4 hrs) compared to DMSO treated cells, particularly for loci up to 20Mb apart (Figure 1 K, L). Compartment strength partially recovers by late G1 (*t* = 8 hrs). We observed no change in chromosome folding at the TAD or loop level upon Topo II inhibition by ICRF-193 in either the AS or MR experiments (Figure S1M, N). In summary, Topo II activity is required for correct timing of dissolution of the mitotic state and establishment of interphase compartments.

**Disruption of compartmentalization with Topo II inhibition can be observed by confocal microscopy**

We next tested whether a delay in compartmentalization with Topo II inhibition was also observable by microscopic analysis of the nuclear localization of two histone modifications: acetylation of histone H3 lysine 27 (H3K27ac), and trimethylation of H3 lysine 9 (H3K9me3)) enriched in the A or B compartments, respectively [51,52]. We fixed HeLa S3 cells to coverslips at *t* = 4 hrs and *t* = 8 hrs after mitotic release for confocal microscopy, followed by immunostaining to label H3K9me3 and H3K27ac. We also stained cells with DAPI to mark the DNA. In the DMSO treated cells, the H3K9me3 signal is highest at the periphery, as expected (Figure 1M, Figure S1Q) [53-57]. H3K27ac is found in puncta in the interior of the nucleus, as expected for active chromatin (Figure 1M, Figure S1Q) [53,55-57]. We find that ICRF-193 treatment during G1 entry significantly increased the fraction of H3K27ac regions that contain smaller H3K9me3 regions in early G1, corresponding to a lower compartment strength observed by Hi-C as compared to DMSO treated cells (Figure 1M, N). In addition, ICRF-193 treatment increases the fraction of H3K27ac signal at the nuclear periphery compared to DMSO treatment at both timepoints (Figure 1O, Figure S1T-V).

**Topoisomerase I activity is not required for compartment establishment**

Next, we investigated whether changes in DNA supercoiling due to loss of Topoisomerase I (TOP1) activity, which nicks DNA rather than making double strand breaks, also results in decreased compartment strength [1,46,58,59]. We treated AS or MR HeLa S3 cells with 5uM camptothecin for four or six hours, respectively, to inhibit TOP1 and found that there was no change in compartment strength when TOP1 was inhibited during G1 entry, while compartment strength was increased when AS cells were treated

with camptothecin, likely due to a G1 cell cycle arrest upon camptothecin treatment (Figure 2A-J, Figure S2A-H) [47,60].

**ICRF-193 induced delay in compartment establishment is independent of transcription**

Transcription inhibition has been shown to perturb DNA supercoiling in interphase cells in a Topo II-dependent manner, and recent studies have shown that blocking RNA Pol II activity has a small effect on establishment of TADs and loops upon mitotic exit, but has little effect on compartment strength [43,46,61]. This led us to the examine whether the structural defects that we observe with Topo II inhibition are related to transcription induced changes in folding, thereby interfering with reformation of G1 structure. We released HeLa S3 cells from mitosis in the presence of Triptolide (TRP) and 5,6-Dichloro-1-beta-Ribo-furanosyl Benzimidazole (DRB), which inhibit transcription initiation and elongation, respectively [62]. (Figure 2K). We found that transcription inhibition results in a 30-minute delay in mitotic exit, as measured by DNA content, so to control for this, all samples with TRP + DRB (Txn Inhib) are collected 30 minutes later than untreated samples (Figure 2J, L) [63]. By Hi-C, transcription inhibition alone did not result in changes in intra-chromosomal compartment strength at any distance, and transcription inhibition did not change the ICRF-193 phenotype of decreased compartment strength in early G1 (Figure 2 M-Q, Figure S2I-N).

**Topo II inhibition must occur early during mitotic exit to delay compartment re-establishment**

We next tested whether the increase in compartment strength in late G1 was due to reduced ICRF-193 potency during the six-hour treatment (Figure 3A). To address this, we re-added DMSO or ICRF-193 every two hours throughout the time course and collected cells in late G1 (*t* = 8 hrs) (Figure 3B). These experiments were performed without G1 sorting, resulting in slightly larger number of cells with a G2 DNA content in populations with ICRF-193 treatment (Figure 3C). We observe the same phenotype in the late G1 (*t* = 8 hrs) timepoint with ICRF-193 added once or re-added every two hours (Figures 3D-G), therefore the recovery in compartment strength is not due to loss of potency of the inhibitor.

To determine whether there is a specific transient state in early G1 that requires Topo II activity, we added ICRF-193 at different times post mitotic release. Comparison of the compartment strength in both the A and B compartments between ICRF-193 and DMSO treated cells shows the largest difference for the earliest sample where ICRF-193 was added at *t* = 2 hrs, while ICRF-193 addition at *t* = 3 hrs and *t* = 4 hrs reduced the effect on compartment establishment (Figure 3 H-N, Figure S3J-O).

**Topo II inhibition changes DNA morphology and Topo IIα localization in early G1**

Individualized mitotic chromosomes display relatively high contrast when stained with DAPI, which we quantified by calculating the contrast of DAPI signal at a 10-pixel distance (Figure S3P, Q) [64]. As cells exit mitosis, this contrast reduces significantly as chromosomes become decondensed. In the presence of ICRF-193 treatment during mitotic exit (starting at *t* = 2 hrs) we observe a smaller decrease in DAPI contrast in

early G1 ($t$ = 4 hrs) as compared to control cells. Additionally, we find that endogenously tagged TOP2A-Venus signal has significantly higher contrast in G1 cells with ICRF-193 treatment, with axial TOP2A staining observed in some cells (Figure S3P, R, see methods).

**Analysis of co-occurring interactions in single cells shows retention of mitotic interactions in ICRF-193 treated cells**

Our data indicate that there is a Topo II dependent transition in chromosome folding as cells exit mitosis. The Topo II dependence suggests that this transition involves a change in the topological state of these chromosomes. We and others previously found that analysis of strings of co-occurring interactions in single cells detected by multi-contact 3C (MC-3C), can provide insights into the intermingling and potentially the topological state of chromatin [27,65]. Here we used MC-3C to measure intrachromosomal intermingling as a proxy for self-catenation in mitotic cells and as cells exit mitosis. In MC-3C, conventional 3C is used to generate long strings of multiple fragments ligated together. Each such string represents a series of co-occurring interactions along a three-dimensional “C-walk” through the folded chromosome [27,65]. These long strings of ligation products are sequenced on a PacBio instrument (see methods). Unlike Hi-C sequencing reads, which record only pair-wise interactions, an MC-3C read can record multiple interactions from a single cell.

Previously, we showed that in AS cell populations of mostly interphase cells MC-3C data are consistent with a largely unentangled state of the genome [27]. Given our results

showing a Topo II requirement during mitotic exit, we wanted to measure the catenation/intermingling status of mitotic chromosomes and determine how the catenation state of the genome changes as cells exit mitosis. We collected synchronized HeLa S3 cells for MC-3C at *t* = 0 (prometaphase arrest), *t* = 2 hrs after nocodazole wash-out (anaphase/telophase), and at *t* = 4 hrs/early G1 or *t* = 8 hrs/late G1 with either DMSO or 30uM ICRF-193 added at *t* = 2 hrs (Figure 4A, Figure S4A-C; 3 replicates). All MC-3C analyses were performed on only the first 6 fragments of C-walks >= 6 fragments, to avoid any artifacts due to differences in read length or number of fragments per C-walk between libraries (Figure S4D,E). MC-3C data recapitulate the Hi-C results in terms of differences in compartmentalization and cis/trans ratio between cell cycle states and with ICRF-193 treatment (Figure 4B).

We next determined the distribution of genomic distances between interacting pairs within C-walks (Figure 4C). We extracted direct pairwise interactions, i.e., adjacent fragments within a C-walk, from MC-3C data. Pairwise interaction distance distributions for *t* = 4 hrs and *t* = 8 hrs DMSO treated cells were similar to previously published MC-3C results in AS HeLa S3 cells, and Hi-C data (Figure 4C, D) [27]. In the prometaphase sample, the pairwise log-distance distribution shows a main peak at 6-7Mb. The most apparent shift as cells enter G1 is loss of mitosis-specific long-range interactions, and a gain in interactions at the TAD (peaks at 200-400kb) and compartment scale (peaks at 10-15Mb). In the ICRF-193 treated cells, this shift occurs more slowly, and particularly at the early G1 timepoint there is a remnant of the mitotic interactions (~10Mb peak, which is smaller than the DMSO compartment scale peak). The same progression and

effect of ICRF-193 is observed for the total span (the largest separation of any two fragments within a C-walk) covered by each C-walk (Figure S4F,G) [27]. Together, these results confirm that ICRF-193 treated chromosomes retain mitotic characteristics in early G1.

**Mitotic chromosomes are intra-chromosomally intermingled**

MC-3C data can tell us about intermingling between chromosomal regions by exploring the subset of C-walks that detect interactions between two distal chromosomal domains. We previously showed by simulation that in the absence of entanglements this interaction surface will be locally relatively smooth, and the two domains only weakly intermingle [27]. In the presence of random strand passage, resulting in catenations between distant domains, the surfaces will become extensively intermingled, and this will affect the composition of the C-walk between the two domains. Thus, we refer to a Topo-II dependent increase in intermingling as emergence of catenations. C-walks at an intermingled surface will include steps that go back and forth between the two domains, while for C-walks at more smooth surfaces most steps are within each domain, with only one step between the two domains (Figure 4E) [27].

We used MC-3C to measure the extent of intrachromosomal catenations in mitotic cells and as cells exit mitosis. We calculated the Intermingling Metric (IM) as the fraction of C-walks that transit between two regions of a chromosome more than once, with 5 fragments in one region and 1 fragment in the other region. We did this as a function of the genomic distance between the regions, defined as the largest step size ($x$) of each

C-walk (Figure 4F,G). The C-walks were binned into overlapping (sliding) windows based on the size of their largest step, and the IM was calculated for each window, for a range of window sizes (Figure 4H). We first measured the IM in control (DMSO treated) cells during mitotic exit. For each timepoint, we plotted the IM as a heatmap organized by the distance between two interacting domains (as calculated by the window midpoint) on the *x* axis vs window size over which the IM was averaged on the *y* axis (Figure 4H, diagonal). Comparing the $t = 0$ prometaphase sample to late G1, we find that prometaphase chromosomes have a higher IM, with ~60% of C-walks containing more than one step connecting the two regions for most distances between two regions. Domains separated by 10-13Mb and 12-22Mb display particularly high levels of the IM at small window sizes, which merge together at large window sizes into a peak from 12-22Mb. In late G1, the IM is significantly lower, with ~50% of C-walks with more than one step between the two regions. The effect size observed here is in line with what was observed in polymer simulations between entangled and unentangled surfaces [27].

Previously we found by simulation that when two domains are strongly catenated and, therefore, intermingled, the number of interdomain steps is predicted to be equivalent to what is observed in permuted C-walks i.e., C-walks where the order of the fragments within each C-walk is shuffled [27]. To compare the experimental IM to the IM obtained from 100 such permutations for each sample, we plotted the IM at just one window size as a function of genomic distance between loci as line plots (Figure 4H, lower triangle). We show the 12Mb window size in the line plots in the main figure, and the 4Mb window size line plots are included in Figure S4N. For both prometaphase and late G1 there are

fewer inter-region steps in the experimental C-walks as compared to what is observed in the permuted C-walks (Figure 4H, bottom right, permuted C-walks indicated by red arrow). This means that the order of the fragments in both prometaphase and late G1 C-walks is not random. Previously we showed that the relatively low intermingling level of the late G1 C-walks is consistent with an unentangled state (Figure 4H, bottom right line plot, unentangled late G1 C-walks indicated by blue arrow) [27]. However, the IM for the experimental prometaphase C-walks is closer to the IM for permuted prometaphase C-walks, and higher than the G1 C-walks (Figure 4H, bottom right line plot, partially intermingled prometaphase C-walks indicated by purple arrow). This result shows that chromosomes transition from a relatively intermingled to a relatively unmingled state during mitotic exit.

Next, we investigated when during mitotic exit intermingling is lost. Heatmaps of the log2 fold-change in the IM between timepoints show that the IM decreases quickly as cells exit mitosis (Figure 4H, upper triangle). At $t$ = 2 hrs (consisting of mainly anaphase/telophase cells), the IM is already greatly reduced compared to prometaphase at all distances. At the $t$ = 4 hrs early G1 timepoint the IM further decreases compared to $t$ = 2 hrs anaphase/telophase, particularly at distances of 12-22 Mb between interacting domains (Figure 4H, lower left triangle, see bracket). This is the same distance range that has the highest level of the IM in the prometaphase sample, and corresponds to the distance where we observed changes in compartment strength with ICRF-193 treatment by Hi-C. However, the IM increased slightly for domains separated by less than 10 Mb in $t$ = 4 hrs early G1 compared to $t$ = 2 hrs

anaphase/telophase. By *t* = 8 hrs (late G1), the IM was at the lowest level across most window size ranges and distances compared to the earlier timepoints, except for the longest-range interactions above 22Mb apart, which show a slight increase compared to *t* = 2 hrs anaphase/telophase and *t* = 4 hrs early G1 samples. Examination of the line plots at the 12Mb window size throughout the time-course shows that the largest change in the IM occurs within the first two hours, as cells go through anaphase and telophase [47], with further changes from *t* = 2 hrs to *t* = 4 hrs, at the distance of 12-17 Mb (Figure 4H, second column, see bracket).

**Chromatin is more catenated within chromosomes in mitosis than in G1**

We next investigated the effect of Topo II inhibition on the changes in the IM during mitotic exit. ICRF-193 was added at *t* = 2 hrs after sister chromatids had separated, and therefore the first timepoint at which it is possible to observe the effect of Topo II inhibition on intermingling is *t* = 4 hrs. We first compared the IM from ICRF-193 treated cells to the same timepoint of DMSO treated cells by visual inspection of their respective IM heatmaps (Figure 4 H, I). ICRF-193 treatment reduces the loss in the IM observed from *t* = 2 hrs to *t* = 4 hrs in the DMSO treated sample at the distances of 10-13 Mb and 20-23 Mb with small window sizes, and 12-22 Mb with large window sizes. However, by late G1 the IM at all distances and size ranges is similar to the DMSO treated sample even with ICRF-193 treatment, similar to the compartment strength recovery by t = 8hrs observed by Hi-C.

Comparing these heatmaps directly by calculating the log2 fold-change (FC), we observe that in early G1 the IM is retained with ICRF-193 treatment at the same interaction distances which have a higher IM in the *t* = 2 hrs anaphase/telophase sample compared to *t* = 4 hrs early G1 DMSO (12-22 Mb). The size range where the IM is retained into early G1 upon ICRF-193 treatment corresponds to the size range where differences in compartment strength were observed by Hi-C. Therefore, a transition in the IM from *t* = 2 hrs anaphase/telophase to *t* = 4 hrs early G1 is blocked with Topo II inhibition by ICRF-193. Line plots of the 12Mb window IM profile confirms this retention of intermingling in the *t* = 4 hrs early G1 ICRF-193 sample from 12-17 Mb. The IM in the *t* = 8 hrs late G1 ICRF-193 sample is similar to the *t* = 8 hrs late G1 DMSO sample at all distances of interacting regions. From these results, we propose that mitotic chromatids contain intra-chromosomal catenations, which require Topo II activity for resolution as cells go through anaphase and telophase and then enter G1. Retention of mitotic catenations into early G1 in the Topo II inhibited cells is correlated with weaker compartmentalization.

**Polymer models of G1 entry without Topo II activity suggest self-entangled mitotic chromatids**

We used polymer modeling to test whether the kinetics of chromosome decondensation and the establishment of compartments depend on the topological state in mitosis. To this end, we started simulations with mitotic chromosomes that either do or do not have intra-chromosomal catenations, and simulated expansion of 90Mb chromosomes without strand passage (as in ICRF-193 treated cells). (see Methods). The mitotic

chromosome was modelled by a dense array of condensin II loops (400kb average size) further confined within a cylinder to reflect chromatin condensation [50]. We considered different topologies of the mitotic chromosome: a “non-catenated state”, with loops not catenated with each other, and a “catenated state”, where loops are catenated; this state was prepared by allowing strand passage. As a quantitative measure of loop catenation we computed a matrix of pairwise linking numbers between the loop pairs (Figure 5A). In the catenated state most of the loops (~66%, Figure 5A) are catenated with others at a mean distance of ~9Mb, which corresponds to the typical size of the mitotic layer (genomic position of the peak at the contact probability, Figure 5D). Despite different topologies, the two mitotic states – catenated and non-catenated - produced equivalent contact probability curves *P(s)* (Figure 5D) and similar contact maps with a characteristic band (Figure 5A), similar to experimental mitotic Hi-C maps (Figure S2D,O). In this way, we were able to specifically test the effect of different topological states of mitotic chromosomes on their interphase properties, while ensuring that all other parameters of mitotic folding were held constant.

G1 entry without strand passage was modeled as the expansion of condensed mitotic chromosomes into the larger volume occupied by interphase chromosomes, using time-calibrated simulations (see Methods). Chromosomes expansion was evoked by release of (a) the cylindrical constraints and (b) condensin loops. Compartment interactions and active loop extrusion were added in the second stage upon release of condensin loops as described in the Methods. Topo II inhibition was modelled by a high excluded volume

barrier between the monomers and short polymer bonds (see Methods) that prevented strand passage and ensured conserved polymer topology.

We observed very different final states when starting from catenated or non-catenated mitotic states. When initiated from a non-catenated state, TADs and compartments can form in G1, even without strand passage (Figure 5B, left). In contrast, when the condensin loops of mitotic chromosome are catenated, mitotic exit without strand passage results in a retained mitotic band of interactions close to the diagonal (Figure 5B, right), weaker compartmental interactions, yet TADs similar to those in the catenated chromosomes (Figure 5B, C). The mitotic band, visible on the simulated interphase contact map formed from the catenated mitotic state, and absent for the non-catenated mitotic state, closely resembles Hi-C patterns seen in Topo II inhibition experiments (Figure 1G). Simulations show that mitotic morphology, seen as the shoulder on *P(s)* in both experiments and the mitotically catenated model, is retained due to residual entanglements between originally catenated loops (Figure 5E). In the absence of Topo II activity, such entanglements cannot be resolved and prevent full opening of chromosomes. This further prevents establishment of long-range interactions between homotypic compartments, and prevents loss of mitotic A-B interactions, thus weakening compartmentalization, consistent with experiments. Thus, simulations suggest that retention of mitotic-like morphology and weaker compartmentalization upon Topo II inhibition during mitotic exit indicate a highly self-entangled mitotic state.

Further evidence of entanglement in the mitotic state comes from observed territoriality of chromosomes upon exit from the entangled, but not from the unentangled mitotic states, as quantified by the cis/trans ratio in simulations and the MC-3C data (see Methods). Simulations that start from catenated and non-catenated mitotic chromosomes, with inhibited strand passage, yield very different cis/trans ratios in the subsequent G1 phase. We calculated cis/trans ratios as a function of time, for the two initial states. (Figure 5F). After several dozen minutes, the cis/trans ratios of chromosomes expanded from a non-catenated mitotic state fall below the interval observed in experimental MC-3C generated pairwise interaction maps for mitotic exit with ICRF-193 treatment (see Fig. S6R for chromosome-wise cis/trans values computed from MC-3C experiments). At the same time, territoriality of chains expanded from a catenated mitotic state quickly saturates at values close to those observed in the experiment. This agreement between experiments and simulations provides more evidence in support of mitotic entanglements.

**A two-stage exit allows chromosomes to transition from an entangled mitotic to an unentangled interphase state.**

How can chromosomes transition from an entangled mitotic state into a largely unentangled G1 state, while establishing proper interphase organization? Our goal is to reproduce two global features of interphase chromosome organization: (i) the fractal (crumpled) globule intra-chromosomal organization evident in the slope of the *P(s)* curve ( -1..-1.2 slope); and (ii) chromosome territoriality (measured by the cis/trans ratio). The fractal globule state is evident from the -1… -1.2 slope of the P(s) curve, and

is observed in cohesin depletion experiments where the slope of *P(s)* plateaus at -1…-1.2 for *s* up to several megabases of genomic distances [66, Hsieh, 2021 #717,67]. This is a signature of a compact and unknotted polymer state with a fractal dimension close to $d_f \approx 3$ and known as fractal (crumpled) globule [31,68-71]. Importantly, the presence of a fractal globule is strong evidence of the unentangled state of interphase chromosomes.

How can these interphase features be achieved when starting from a mitotic chromosome with catenated loops, and subject to Topo II activity? First, we examined expansion of entangled mitotic chromosomes in a single stage (one-stage model), i.e., via simultaneous release of condensin loops, which occurs by telophase [47,72], and release of cylindrical confinement subject to active Topo II (low barrier to strand passage) (Figure 6A-C). To better see the slops of *P(s)* we don't include formation of cohesin loops in these simulations. Simulations show that while the mitotic state rapidly expands, the fractal globule state cannot be established, as evident from the slope of the P(s) curve approaching -1.5, far below the experimentally observed slope of -1 - -1.2 (seen in the absence of cohesin). This behavior is expected as high Topo II activity turns the chain into a topologically unconstrained and highly entangled ideal chain (Figure 6A) [73]. Furthermore, we see that chromosomal territoriality falls below the levels observed in MC-3C for WT interphase cells (Figure 6C and Figure S6R). Addition of loop extrusion by cohesin to simulations achieved a higher level of territoriality (~55% increase at 3 hours of expansion (Figure 6C)), close to the MC-3C experiment, yet the fractal globule cannot be reproduced. Together, these results indicate that while random Topo II activity allows entangled mitotic chromosomes to expand, it precludes

establishment of chromosome territories and formation of the fractal globule state, as generally expected for topologically unconstrained polymers [31].

Since the one-stage exit from an entangled mitotic state does not reproduce the features of an unentangled interphase, we next ask whether exit with differentially regulated Topo II activity can effectively disentangle the mitotic state. We suggest that maintaining mitotic loops while allowing loops to decondense could bias Topo II towards decatenation of the loops, leading to formation of a transient unentangled state. Further expansion from this state could lead to formation of the interphase chromosomes without requiring additional Topo II activity.

On the basis of this idea, we propose a two-stage expansion process (Figure 6D). During stage 1, Topo II is active and the cylindrical constraints on the mitotic chromosome are released, while mitotic loops are still present. Simulations show that the first stage results in directed decatenation of condensin loops. A simulated chromosome is reminiscent of a swollen bottlebrush, which gradually lengthens, as more and more loops become decatenated from the others (Figure S5B). These morphological changes are accompanied by a gradual dissolution of the mitotic band (Figure S5A). Decatenation of condensin loops in the first stage is evident from the matrices of linking between the loops (Figure 6D,E, see also Figure S5C). Catenations are gradually lost during the first stage: In 10 minutes of the first stage around 50% of mitotic catenations are removed, while at ~1 hour after the expansion the average amount of catenations per one loop reaches the steady-state, i.e. the number of newly

formed catenations matches the number of removed catenations (Figure 6E, Figure S5C). This topological steady-state features around 10% of loops that remain catenated with the other loops on the same chromosome, and only 2% of loops which become catenated with loops on other chromosomes (Figure 6E). The first stage resolves mitotic entanglements because steric repulsion between the expanded loops creates forces that tend to segregate them, and Topo II activity then leads to loop decatenation.

At stage 2, the mitotic loops are released and Topo II activity is decreased by more than ≈7-fold (see Methods). Active cohesin loop extrusion and compartmentalization are also introduced at stage 2 (Figure 6D), yet we first consider simulations without cohesin loops to better see the fractal globule. Simulations show that the remaining level of catenations is negligible and chromosomes form the fractal globule with a characteristic slope of $P(s)$ $-1.2$ from $50$ kb to $4$ Mb (Figure 6G, 7E,F) [66,67,69,74-76] The fractal globule is also evident from the visual comparison of snapshots of chromosomes colored along the chain, for the two- and one-stage expansion processes (at $t$=2h). The fractal globule is known to produce clear "territoriality" of genomic segments within a chromosome, as seen for the two-stage exit, in contrast to mixing of segments in the case of the one-stage exit [26] (Figure 6H). Simulations also show the fractal globule state can be formed even in the presence of some low-level of Topo II activity (occasional strand passage) in the second stage, as long as the condensin loops are largely decatenated in the first stage (Figure S6S). Thus, the proposed two-stage mechanism allows for robust directed decatenation of mitotic loops via biased strand passage activity of Topo II during stage

1, while mediating the establishment of the fractal globule within each chromosome during stage 2.

Furthermore, we find that the territoriality of chromosomes after the two-stage exit matches the observed cis/trans values of the Control (DMSO treated) interphase, overlapping with the interval of experimental MC-3C values for different chromosomes (Figure 6F, Figure S6I-L). We find that the cis/trans levels at the second stage drastically depend on duration of the first stage (Figure 6F), which controls the number of residual catenations (Figure 6E). The more remaining mitotic catenations propagate into the second stage, the larger the territoriality levels. However, for *t*=2h of the first stage, when massive decatenation results in a practically unentangled state, (Figure 6G), the level of territoriality decreases to the lower bound of the experimentally observed cis/trans ratio in the second stage. This is not surprising, since large unknotted non-catenated rings, residing in the unentangled state, show weak territoriality [75]. Since relatively short chromosomes are being simulated they should be compared to the lower range of experimental cis/trans for shorter chromosomes (Figure S6R). This suggests that other aspects of mitotic exit, such as interactions with lamina, could help establish stronger territoriality.

We see other features of the interphase chromosomes reproduced by the two-stage exit when loop extrusion by cohesin and compartmental interactions are turned on at the second stage. In the course of the second stage the chromosomes become more compartmentalized, as evident from the contact maps and the saddle plots (Figure S6A-

D). We also see evidence of gradual transition from the mitotic dense loop array to the interphase sparse array of loops. This is evident in the deepening of the “dip” on the slope of the *P(s)* curve (Figures S6E-H). The same deepening effect is observed in experimental *P(s)* scalings and is associated with the general polymer relaxation of the linkers between topologically repelling loops [77]. Taken together, the two-stage mechanism of mitotic exit with controlled Topo II and decondensation activities facilitates large-scale chromosome disentanglement, while allowing the establishment of interphase organization with its hallmarks: the fractal globule, chromosome territoriality and stronger compartmentalization.

**Topo II activity is required for increased compartment strength upon loss of cohesin**

It has been observed that total TOP2A levels and activity are higher in mitosis than in late G1, consistent with the two-stage model (Figure 6D) [78-81]. However, some level of Topo II activity is detected throughout the cell cycle [22,81,82]. This active Topo II does not appear to result in new entanglements during interphase, such as between newly interacting AA and BB domains (Figure 4H) [27]. Simulations show that extensive entanglement would be expected from highly active Topo II acting with random directionality within a crowded nucleus [27,83], see Figures 6A-C. The level of Topo II protein during G1 may simply be sufficiently low to prevent formation of new catenanes, as supported by the polymer simulations described above. However, we also considered whether the activity of Topo II is regulated during G1. Specifically, yeast minichromosome experiments have shown that condensin-mediated loop extrusion

biases Topo II towards disentangling minichromosomes [84,85]. Computational modeling also suggests that a mechanism of loop extrusion, by cohesin or condensin, could bias Topo II towards untangling chromosomes [83]. Together, these observations led us to hypothesize that the cohesin complex may play a role in controlling Topo II activity during interphase to help maintain a largely unentangled genome.

To test this hypothesis, we used the previously described HCT116 cell line carrying an auxin inducible degron (AID) and mClover fusion of RAD21, a subunit of the cohesin complex, and the OsTIR1 adapter protein (HCT116 + RAD21-mAC cell line) [66,86-88]. Using this system, we measured how chromosome folding is affected by the combined loss of Topo II activity and cohesin by Hi-C and MC-3C. We treated asynchronous (AS) HCT116 + RAD21-mAC cells, which are mainly in the G1 phase of the cell cycle, with 30uM of ICRF-193 to inhibit Topo II or DMSO, and/or 500uM Auxin (Indole-3-acetic acid, IAA) to degrade RAD21 for two hours (Figure 7A, Figure S7A). Following fixation, the cell populations were sorted for G1 DNA content, and +/- mClover expression (Figure S7B,C).

By Hi-C, we find that IAA treatment alone reduces loop strength, as previously published [66], while ICRF-193 treatment alone has no effect on looping interactions (Figure 7B), as was observed for both AS and MR experiments in the HeLa S3 cell line (Figure S1N). As previously observed, we find that while short-range interactions are decreased, long-range compartment specific interactions are increased with RAD21 degradation in the IAA treatment (Figure 7C, D) [66]. The loss of cohesin-mediated loop

extrusion can be observed by a loss of contacts with a peak in the derivative of *P(s)* at ~100 kb genomic separations, and loss of TADs on 50kb binned heatmaps (Figure 7E, F, Figure S7D-F,H) [77,89,90]. As previously observed, we find that compartment strength is increased with RAD21 degradation (Figure 7G, H, FigureS7G) [66,89,90]. However, the compartment strength increase observed with IAA treatment is partially blocked by the addition of ICRF-193, particularly in the B compartment. Treatment with ICRF-193 alone has only minimal effects on compartment strength, as also observed in the AS HeLa S3 cell line (see Figure 1K,L). Therefore, Topo II activity contributes to this transition in chromosome folding at the compartment scale upon loss of cohesin.

**RAD21 degradation increases entanglement between distal B compartment domains**

We next investigated whether RAD21 degradation with or without ICRF-193 treatment causes changes in entanglement between compartmental domains, as measured by MC-3C. The distribution of the spans of C-walks shows a loss of shorter C-walks (within one TAD or compartment domain) and an increase in longer-range C-walks (between one or more TADs or compartment domains) upon loss of cohesin (Figure 7I, Figure S7N). ICRF-193 treatment alone does not affect the C-walk span distribution, but ICRF-193 treatment combined with IAA shows a slight increase in shorter C-walks and decrease in longer C-walks compared to IAA alone (Figure 7I, Figure S7N). Loss of TADs and CTCF loops with RAD21 degradation is apparent by a decrease in the peak at 200-300kb in the pairwise distance distribution plot (Figure 6J, Figure S7O). Again,

IAA + ICRF-193 treatment results in less of a change than IAA alone compared to the control.

Next, we measured the IM as described in Figure 4, for 2-50Mb separations of interacting regions for each condition. When all compartment types were considered together, there was a significant change in the IM with cohesin degradation above 30Mb separation compared to the control (Figure 7K). This difference was mainly due to increases in the IM between B compartments at these distances of separation, or between A and B compartment domains, but such increase was not observed between A compartment domains, (Figure 7L, Figure S7Q,R). Cohesin degradation upon IAA treatment causes B-B intermingling that is comparable to the permuted walks where the order of all steps is shuffled randomly (Figure S7R). The IM with ICRF-193 treatment is similar to the control intermingling levels for all compartment types, and IAA + ICRF-193 results in IM values which are only slightly higher than the control and are significantly lower than IAA alone. We conclude that long-range interacting domains, particularly B compartment regions, become more entangled upon the loss of cohesin in a Topo II dependent manner. These results indicate that the presence of cohesin effectively prevents unbiased entanglement within the B compartment during maintenance of normal G1 chromosome organization.

## DISCUSSION

We show that unlike interphase chromosomes, mitotic chromosomes are entangled at the multi-megabase scale. Most of these entanglements are removed quickly as cells

exit mitosis during anaphase and telophase, driven by chromatin expansion, with remaining entanglements removed during early G1. Failure to remove entanglements, when Topo II activity is inhibited, leads to delayed dissolution of the mitotic conformation, and delayed establishment of heterochromatin and euchromatin compartments upon G1 entry. The interphase state remains unentangled because topoisomerase II activity is reduced, and through a process that involves cohesin mediated limitation of Topo II activity at least in the B compartment.

**The mitotic chromosome is internally entangled**

Whether intra-chromosomal entanglements occur in mitotic chromosomes has long been an open question in the field, due to an inability to directly measure them in endogenous chromosomes. Entangled mitotic chromosomes are predicted to form a stiffer structure than unentangled chromosomes, which may be important for ensuring proper chromosome segregation[29]. An unentangled mitotic state has been predicted based on computational models, which show that expansion from mitotic chromosomes with mutually non-catenated loops and inactive topo-II ensures the formation of an unentangled and territorial interphase conformation [30,31]. In contrast, mitotic self-entanglements have been suggested based on classical and more recent experiments and early models which proposed the importance of Topo II for chromosome compaction and decompaction during mitotic entry and exit [29,32,91-94].

Other studies which used Hi-C to inform computational models of mitotic chromosome folding, required Topo II activity in the models and observed mixing at the scale of

<10Mb, which is consistent with chromosome entanglements, but these studies did not comment on the topological state within chromatids [48,50,95,96]. In addition, in vitro micro-mechanical studies of mitotic chromosomes have shown that chromosome elasticity can be modulated by the addition of Topo II, with intra-chromatid entanglement contributing to mechanical stiffness of mitotic chromosomes required for accurate chromosome segregation [29]. A recent study using in vitro mitotic chromosome reconstitution in Xenopus egg extracts showed that in histone depleted chromosomes, Topo II activity is required to increase chromosome thickness when condensin is present, but results in inter-chromosome entanglements when condensin is depleted [94]. This study then went on to suggest a model of intra-chromosomal entanglements mediated by Topo II directed by condensin to form mitotic chromosomes, which is consistent with our entanglement measurements during mitosis [94].

In this study, we use MC-3C and Topo II inhibition to show that mitotic chromosomes are entangled, and that these entanglements are removed in a Topo II dependent manner upon G1 entry. Our polymer simulations of G1 entry support this experimental data that mitotic chromosomes are internally entangled, as unlike endogenous chromosomes, non-entangled chromosomes in simulations do not require Topo II activity to expand and form strong compartments. In contrast, simulated chromosomes with mutually catenated loops can neither expand nor fully compartmentalize without Topo II activity. In light of our simulations, the experiments are consistent only with an initially entangled mitotic state. Interestingly, while ICRF-193 treatment results in recovery to nearly control compartment strength by late G1 (8hrs) in experiments,

simulations recover with much slower kinetics without Topo II activity. This difference suggests that there must be an additional active mechanism within the nucleus that can reduce chromosome intermingling in a Topo II independent manner.

**Two-stage exit from mitosis**

Formation of interphase organization from an entangled mitotic chromosome poses a serious challenge: While Topo II activity allows expansion and compartmentalization, at the same time it prevents the establishment of hallmarks of the interphase organization such as chromosome territories and the fractal globule state. Polymer simulations show that this paradox can be resolved by a two-stage mitotic exit.

In the first stage, decompaction of mitotic chromosomes with mitotic (condensin) loops still present produces a swollen bottlebrush conformation. Loops in this state repel each other, biasing Topo II towards decatenation. This stage requires Topo II activity prior to dissociation of condensins. This intermediate swollen bottlebrush state is likely present until telophase onset. Interestingly, an extended mass of several chromosomes observed by microscopy suggests that the anaphase-telophase transition is linked to decompaction and likely decatenation [72]. Simulations suggest that Topo II inhibition would block chromosomes in this transient state, with weak compartments and retained mitotic structure, consistent with experimental results.

In the second stage, chromosomes which are largely disentangled at the first stage, expand upon loss of condensin loops with a reduction in Topo II activity. Reduced Topo

II activity (i.e. reduced strand passage) allows for maintenance of the largely unentangled interphase state and results in formation of the fractal globule and establishment of chromosomal territories. Importantly, the second stage does not require complete loss of Topo II activity, but instead can proceed with ~7 fold reduced probability of strand passage compared to the first stage.

**Cohesin biases Topo II towards disentanglement of interphase compartment domains**

Recent computational studies have proposed that loop extrusion by SMC complexes may bias Topo II towards disentanglement, or decatenation [97,98]. An elegant study in budding yeast on the topological state of yeast minichromosomes has identified a role for the condensin complex in this process [84,85]. We find that in cohesin depleted G1 cells, both compartment strength and long-range intra-chromosomal entanglement increases in a Topo II dependent manner. Topo II is known to be active during interphase [21,22], but in the presence of cohesin we find that it does not lead to high levels of entanglement (Figure 7K,L). We interpret these results to mean that Topo II activity is somehow biased by the presence of the cohesin complex, such that it preferentially decatenates interphase compartment domains, at least in the B compartment.

One hypothesis is that Topo II activity may be controlled by a direct interaction with the cohesin complex, such that both complexes must be localized to a catenated site on the chromosome in order for Topo II to be active, allowing cohesin to directly affect the

direction of the strand passage, leading to more decatenation. A second hypothesis is that active loop extrusion by cohesin makes the chromosome more compact at the level of TADs, or within compartment domains [90,99-101]. The short-range compaction along the linear genome would result in smoother, or less rugged interfaces between chromosomes [102] and between compartment domains and could by itself lead to domain decatenation by Topo II, without requiring physical interactions between the machines. Upon loss of cohesin, the short-range compaction is lost, and interfaces between compartment domains may become more rugged, with increased surface area, leading to a higher probability that Topo II activity would lead to catenation between the domains. Heterochromatin in the B compartment has been shown to have a higher chromatin density than euchromatic regions, which may contribute to the increased probability of entanglement in this compartment type when Topo II acts indiscriminately [103]. A third hypothesis is that cohesin mediated looping is converting global features of chromosome topology into local DNA features, so that Topo II can act on these in a non-random way. It is known that Topo II has some directionality and proof-reading activity due to DNA supercoiling when it acts on circular plasmids [104-106]. However, it is not known how this activity pertains to global chromosome topology when the substrate is chromatinized DNA. Cohesin may generate local chromatin features such as crossovers that reflects features of the global structure, either by localizing a knot as proposed by Orlandini et al (2019) [83], or by some other mechanism. Non-random action of topoisomerase II on such local conformations can then lead to global decatenation.

Taken together, our work shows that cells control the entanglement state of the genome during mitotic exit, with important roles for chromosome loops, chromatin decondensation, and regulation of Topo II activity levels (Figure 7L).

## METHODS:

### Creation of a stable HeLa S3 TOP2A-Venus cell line

The cell line was constructed as described for generation of a stable HeLa S3 NCAPH-dTomato cell line in Abramo et al, 2019 [47]. Briefly, pSpCas9(BB)-2A-Puro (BX459) v.2.0 (a gift from F. Zhang (Addgene plasmid, 62988; RRID, Addgene_62988)) was used to construct CRISPR/Cas vectors according to the protocol of Ran et al [107]. gRNA sequences are provided in Supplementary Table 1. To construct the donor plasmid for C-terminal integration of Venus, pUC19 (Thermofisher, Cat SD0061) was used as the backbone and was constructed using synthesized DNA and homology arms generated by PCR (primers provided in Supplementary Table 2). Genomic DNA from HeLa S3 cells was used as template, and was amplified using Q5 High-Fidelity DNA Polymerase (New England Biolabs Cat M0491S) to generate 800 bp *TOP2A* homology arms. A gBlock containing 5X Glycine linker, Venus, T2A and Hygromycin resistance was synthesized by Integrated DNA Technologies (IDT) (sequence is provided in Supplementary Table 3). Homology arms and gBlocks were cloned into pUC19 by Gibson assembly using NEBuilder HiFi DNA Assembly Master Mix (NEB E2611S). To generate stable cell lines, 5x10^6 cells were electroporated with gRNA plasmids and homology arm donor plasmid. Then, 24h after electroporation, 1ug/ml puromycin selection was added, and, 2d later, 150 ug/mL hygromycin B Gold (Invivogen #

ANTHG1) was added for TOP2A-Venus selection. After 4 d, colonies were picked for further selection in a 96 well plate. The HeLa S3 TOP2A-Venus clone B1 cell line is available on request, with a material transfer agreement from ATCC for use of the original HeLa S3 cell line. Alternatively, constructs will be available from Addgene upon publication to enable the re-creation of the cell line in unmodified HeLa S3 cells.

**Cell Culture**

HeLa S3 CCL-2.2 cells (ATCC, CCL-2.2) with or without TOP2A-Venus were cultured in DMEM, high glucose, GlutaMAX™ supplement with pyruvate (Gibco, 10569010) supplemented with 10% fetal bovine serum (Gibco, 16000044) and 1% penicillin-streptomycin (Gibco, 15140) at 37 degrees C in 5% $CO_2$. HCT116 + RAD21-mAC cells [87] were cultured in McCoy's 5A (Modified) Medium, GlutaMAX™ supplement (Gibco, 36600021) supplemented with 10% fetal bovine serum (Gibco, 16000044) and 1% penicillin-streptomycin (Gibco, 15140) at 37 degrees C in 5% $CO_2$. Topo II inhibition was performed by adding ICRF-193 (Sigma-Aldrich, I4659-1MG) dissolved in DMSO (4mg/ml stock solution) and used at 30uM final concentration in cell culture media. A 30uM dose of ICRF-193 is sufficient to inhibit Topo II, as this dose blocks chromosome segregation and delays mitotic exit when added at t0 (nocodazole wash-out), as measured by cyclin B degradation in HeLa S3 cells and analysis of DNA content by flow cytometry (Figure S1A-G) [38,45,46]. In addition, it has been shown that a five-hour treatment with 35uM ICRF-193 results in an overall loss of DNA supercoiling in RPE1 cells, and blocks changes in supercoiling due to transcription inhibition [46]. ICRF-193 potency was tested for each batch by adding 30uM ICRF-193 or an equal volume of

DMSO at *t* = 0 to a sample of washed prometaphase arrested HeLa S3 cells re-cultured in standard media, and collecting both the floating and adherent cells for cell cycle analysis by PI staining and flow cytometry after four hours. Experiments were only continued if the ICRF-193 at *t* = 0 treatment arrested cells with G2/M DNA content, by inhibiting decatenation of sister chromatids, but the DMSO control allowed the majority of cells to enter G1. Transcription inhibition was performed by adding 25uM Triptolide (TRP) (Millipore, 645900-5MG, stock was 55mM in DMSO) and 200uM 5,6-Dichlorobenzimidazole 1-β-D-ribofuranoside (DRB) (Sigma, D1916-50MG, stock was 70mM in DMSO) and incubating for the indicated times at 37 degrees C in 5% $CO_2$. Auxin induced degradation of RAD21-AID-mClover in the HCT116 + Rad21-mAC cells was performed by adding 500uM 3-Indoleacetic acid (IAA, auxin) (Sigma, 45533-250MG) dissolved in 100% Ethanol, and incubating for the indicated times at 37 degrees C in 5% $CO_2$. The TOP1 inhibitor camptothecin (Sigma-Aldrich, C9911-100MG) was dissolved in DMSO and used at a final concentration of 5uM for the indicated times at 37 degrees C in 5% $CO_2$.

**Mitotic Synchronization and Release Time Course**

Prometaphase synchronization and release of HeLa S3 CCL-2.2 cells for Hi-C, MC-3C, and IF was performed as previously described [47,48]. For all experiments except DAPI and TOP2A-Venus contrast measurements by microscopy, a single thymidine block was used to first arrest cells in S phase: cells were plated at 4x10^6 cells per 15 cm plate in medium containing 2mM Thymidine (Sigma, T1895), and were grown for 24 hours. Next, cells were washed with 1x DPBS (Gibco, 14190144) and standard medium

was added to the plates for 3 hours to allow release from S phase and recovery of cells. For all synchronization experiments, 100ng/ml nocodazole (Sigma, M1404) was added for 12 hours to synchronize cells in prometaphase, by depolymerizing the spindle microtubules. Floating mitotic cells were collected by mitotic shake-off and washed in 1x DPBS (Gibco, 14190144). Mitotic samples were collected directly from washed prometaphase cells and immediately prepared for downstream purposes. The remaining cells were re-cultured in pre-warmed standard medium for synchronous release into G1 and were collected at indicated timepoints post-mitotic release, depending on the experiment. For the *t* = 2 hrs timepoint, both the floating and adherent cells were collected. For timepoints from *t* = 4hrs to *t* = 9hrs, only adherent cells were collected, unless otherwise indicated. For Hi-C, MC-3C, and IF, 30uM ICRF-193 (Sigma-Aldrich, I4659-1MG) in DMSO, or an equal volume of DMSO as a vehicle control, was added at *t* = 2 hours.

**Flow Cytometry**

For cell cycle analysis, approximately 0.25-1x10^6 cells at each timepoint were collected in 15 ml conical tubes. For samples where both floating and adherent cells were collected, the media was first transferred to the conical, then the plate was washed 1x with 1x DPBS (Gibco, 14190144), and then the adherent cells were released using StemPro Accutase (ThermoFisher, A11105-01) or TrypLE Express (ThermoFisher, 12605036). For adherent only samples, the media was instead discarded. Released cells were transferred to the 15 ml conical, and were then washed 1x with 1x DPBS (Gibco, 14190144), and resuspended in 100ul of 1x DPBS. Cells were fixed with 1 ml of

cold 100% Ethanol added drop-wise while vortexing on the lowest setting, to reduce clumping. Samples were then incubated at -20 degrees C for at least 30 minutes, or stored at this temperature until staining was continued. For propidium iodide (PI) staining, fixed cells were washed in 1x PBS (Gibco, 70013-073), and then resuspended in 1x PBS containing 0.1% NP-40 (MP Biomedicals, 0219859680), 0.05mg/ml RNAse A (Roche, 10109169001) and 5 or 50ug/ml propidium iodide (Thermo, P1304MP). The samples were incubated at room temperature (20 degrees C) for 30 minutes, and were then analyzed using a BD LSR II or MACSQuant VYB flow cytometer. Data were analyzed using FlowJo V10.8.1. Viability gates using forward and side scatter area were set on the AS sample in each experiment, and were applied to all of the samples within the set. Doublet discrimination was then performed using forward scatter area vs forward scatter height. DNA content was plotted as a histogram of the PI channel area, the exact channel settings varied depending on the instrument used. For the LSR II, PI was excited by either a yellow laser (561nm), with the PI fluorescence collected with either a 600LP dichroic mirror and a 610/20 filter or a 570LP dichroic mirror and a 580/20 filter, or by a blue laser (488nm) with a 685LP dichroic mirror and a 695/40 filter. For the MACSQuant VYB, PI was excited by either a yellow/green laser (561nm), and the PI fluorescence was collected with either a 586/15 filter or a 615/20 filter, or was excited by a blue laser (488nm) and PI fluorescence was collected with a 614/50 filter. No compensation was required. G1, S, and G2/M gates were set manually on the AS sample and applied to all of the samples within the set to obtain the percentage of cells in each state throughout the experiment. For analysis of RAD21-mAC degradation, cells were fixed and PI stained as for Hi-C or MC-3C with 1% Formaldehyde (Fisher, BP531-

25) +/- 3mM DSG, to prevent loss of free RAD21-mAC due to ethanol induced cell permeabilization (see below for full method). Cells were run on the MACSQaunt VYB, PI was excited by a yellow/green laser (561nm), and the PI fluorescence was collected with either a 586/15 filter or a 615/20 filter, and Clover was excited by the blue laser (488nm), with Clover fluorescence collected with a 525/50 filter. No compensation was required. For analysis of apoptotic cells using Annexin-5 staining, the FITC AnnexinV/Dead Cell Apoptosis Kit (Invitrogen, V13242) was used. Cells were run on the MACSQuant VYB: PI was excited by a yellow/green laser (561nm), and the PI fluorescence was collected with either a 586/15 filter or a 615/20 filter, and FITC was excited by the blue laser (488nm), with FITC fluorescence collected with a 525/50 filter. No compensation was required.

**Hi-C**

Hi-C was performed using the Hi-C 2.0 protocol [44]. For unsorted samples, approximately 5x10^6 cells were fixed in 1% formaldehyde (Fisher, BP531-25) diluted in serum-free media, as previously described. For G1 sorted samples, 10-20x10^6 adherent cells were first removed from the plate using StemPro Accutase (ThermoFisher, A11105-01) or TrypLE Express (ThermoFisher, 12605036), were washed 1x in HBSS (Thermofisher, 14025134), and then were fixed in 1% formaldehyde (Fisher, BP531-25) in HBSS (Thermofisher, 14025134), to reduce clumping during FACS. Formaldehyde fixation was quenched with 0.125M Glycine for 5 minutes at room temp, and 15 minutes on ice. Cells were washed after fixation with DBPS, and the cell pellets were flash frozen in liquid $N_2$ and stored at -80 degrees C.

For G1 sorting, flash frozen cross-linked cell pellets were thawed on ice and were partially permeabilized using 0.1% Saponin in 1x PBS. (Sigma-Aldrich, 47036-50G-F). Cells were then treated with 2mM MgCl2, 100ug/ml RNAse A (conc, Roche, 10109169001) and 50ug/ml conc propidium iodide (Thermo, P1304MP) for 30 minutes at room temperature with gentle mixing. Cells were spun down and resuspended in 1x PBS (Gibco, 70013-073) + 1-3% BSA (Sigma Aldrich, A7906-50G) + 50ul/ml propidium iodide, and were sorted for G1 DNA content for the HeLa S3 experiments, or for G1 DNA content plus or minus mClover (GFP channel) signal for the HCT116 + Rad21-mAC experiments, into PBS + 1-3% BSA using a BD FACS Melody with the following channels: FSC, SSC, PI: 561nm laser, 605LP dichroic mirror, 613/18 filter, Clover (FITC channel): 488nm laser, 507LP dichroic mirror, 427/32 filter or a BD FACS Aria IIu with the following channels: FSC, SSC, PI: 561nm laser, 600LP dichroic mirror, 610/20 filter or 488nm laser, 655LP dichroic mirror, 695/40 filter, Clover (FITC channel): 488nm laser, 502 or 505LP dichroic mirror, 530/30 or 525/50 filter. After sorting, cells were pelleted by centrifugation, flash frozen in liquid $N_2$, and stored at -80 degrees C. Flash-frozen cross-linked cells either with or without sorting were thawed on ice for Hi-C, and were then lysed and digested with DpnII (NEB, R0543M) at 37 degrees C overnight, following the Hi-C 2.0 protocol [44]. The overhanging DNA ends were filled in using biotin-14-dATP (LifeTech, 19524016) at 23 degrees C for four hours, and ligated with T4 DNA ligase (Life Technologies, 15224090) at 16 degrees C for four hours. Chromatin was then treated with proteinase K (ThermoFisher, 25530031) at 65 degrees C overnight to remove all cross-linked proteins. Ligation products were purified by phenol:chloroform extraction with ethanol precipitation, fragmented by sonication, and size-selected using

SPRI beads to retain fragments of 100-350bp. Next, we performed end repair and then selectively purified biotin-tagged DNA using streptavidin coated beads (DYNAL™ MyOne™ Dynabeads™ Streptavidin C1, Invitrogen 65001). A-tailing and Illumina TruSeq adapter ligation (Illumina, 20015964) were performed on the bead-bound ligation products, and samples were amplified using the TruSeq Nano DNA Sample Prep kit (Illumina, 20015964). PCR primers were removed using SPRI beads (1.1x ratio) before sequencing the final Hi-C libraries using PE50 bases on an Illumina HiSeq 4000.

**Hi-C Analysis**

*Read Mapping*

Hi-C data processing was performed as previously described [47]. Hi-C PE50 FASTQ sequencing reads were mapped to the hg38 human reference genome using the nextflow based distiller-nf pipeline, followed by filtering to retain only reads with mapping quality (MapQ) of 30 or higher, and removal of duplicate reads. The resulting filtered reads are referred to as valid pairs [108]. The number of valid pairs was normalized within each experiment using cooltools (v0.5.1) random-sample with the –exact argument on 1kb resolution .cool files [109]. MultiQC was used for quality control of the Hi-C libraries [110]. Read normalized valid pairs were binned into .mcool formatted contact matrices at 1kb, 5kb, 10kb, 25kb, 50kb, 100kb, 250kb, 500kb, and 1Mb using the python package cooler (v0.8.11), and were iteratively balanced (ICEed), while masking the first two bins at the diagonal, which can contain artifactual ligation junctions [111,112]. Hi-C analysis was performed using custom python based Jupyter notebooks utilizing Hi-C specific python

packages such as cooler (v0.8.11), cooltools (v0.5.1), bioframe (v0.3.3) and pairtools (v0.3.0) [109,111-115]. Other python packages used included pandas (v1.4.2), numpy (v1.22.3), scipy (v1.8.0), scikit-image (v0.19.2), seaborn (v0.11.2) and matplotlib (v3.5.2) [116-122]. Examples of custom python scripts used for Hi-C analysis and visualization will be available on github.

*Distance Decay*

Contact frequency (*P*) as a function of genomic distance (*s*) and the derivative (slope) of this *P(s)* curve were calculated using cooltools compute-expected followed by cooltools logbinned-expected using only intrachromosomal reads from the read normalized cooler files, binned at 1Kb [109]. For Hi-C from HeLa S3 cells, only chromosomes without major translocations were used (chr4, chr14, chr1, chr18, chr20, chr21) [48].

*Insulation Profiles*

Diamond insulation score was calculated on 10kb binned .cool files using the cooltools API function calculate_insulation_score, with a 250kb diamond sliding window [109]. Domain boundaries were found by locating minima in each profile, and thresholding using skimage threshold_otsu [121]. Boundaries were then filtered to remove boundaries that overlapped with changes in compartment identity, to analyze TAD only boundary strength. Aggregate insulation plots were made by plotting the average insulation in 500kb windows around all called TAD boundaries in each Hi-C library [120].

*Compartment Analysis*

Active and inactive compartment regions were identified using eigenvector decomposition on 100kb or 250kb binned Hi-C .cool files using cooltools, as previously described [47,109,123]. The eigenvector was phased such that positive values corresponded

to the more gene-dense regions of the genome (the 'A', or active compartment), while negative values corresponded to the gene-poor regions of the genome (the 'B' or inactive compartment). To measure the strength of compartmentalization, we used cooltools saddleplot analysis on observed/expected Hi-C data at a range of distances, as previously described, where the expected matrix corresponds to the average distance decay [47,109,123]. Observed/expected matrix bins within each distance band were sorted and aggregated into 50 bins according to their eigenvalue. Strength of compartmentalization for each distance was calculated as the ratio of AA/AB or BB/AB interactions, where AA is the average of the corner 10 bins with positive, positive eigenvalues, BB is the average of the 10 corner bins with negative, negative eigenvalues, and AB is the average of the 10 bins in the corner with positive, negative eigenvalues.

*Loop pileups*

We called loops on deep HeLa S3 (4DNFIBM9QCFG) or HCT116 + Rad21-mAC Untreated (4DNFIFLDVASC) Hi-C data from the 4DN data portal [66], using cooltools call-dots for the loop pileup analyses, with cooltools v0.4.0 [124]. For the HeLa S3 data, we obtained 13385 total dots, 2359 on the structurally intact HeLa S3 chromosomes. For the HCT116 + RAD21-mAC data we obtained total 3030 dots on all chromosomes. To plot the aggregate looping interactions, we used cooltools snipping to aggregate 10kb cooler files at the intersection of the two loop anchors, and plotted the average observed/expected ratio for each sample [109].

**MC-3C**

MC-3C was performed as previously described, with some changes in the crosslinking and ligation protocols [27]. Cells were collected and fixed following the Hi-C 2.0/MC-3C protocol [27,44], for adherent cells dissociated for G1 sorting as described above (all HCT116 samples, G1 HeLa S3 samples, and adherent population of *t* = 2 hrs HeLa S3 samples), or from suspension cells (*t* = 0 prometaphase and floating population of *t* = 2 HeLa S3 samples), with the following changes: After quenching of formaldehyde crosslinking, cells were washed 2x with DPBS (Gibco, 14190144), and were additionally fixed with 3mM Disuccinimidyl Glutarate (DSG) (ThermoFisher, 20593) diluted in DPBS from a 300mM stock in made with DMSO and incubated at room temperature for 45 minutes. DSG crosslinking was quenched by addition of 0.75M Tris pH 7.5 [125,126]. Cells were pelleted (1000xg) and then washed 2x after fixation with DBPS. Cell pellets were flash frozen in liquid $N_2$ and stored at -80 degrees C until either G1 sorting or starting MC-3C. For MC-3C, flash-frozen G1 sorted or unsorted cross-linked samples were thawed on ice, and followed the Hi-C 2.0/MC-3C protocol through DpnII digestion [27,44]. Importantly, throughout the remainder of the protocol care was taken to reduce pipetting of samples to avoid shearing and damaging DNA at all steps, and mixing was performed by invert mixing and light vortexing only. After DpnII digestion and inactivation, the overhanging DNA ends were ligated using 50uL T4 DNA ligase (Life Technologies, 15224090) at 16 degrees C for 4 hours in a ligation buffer containing 1x Invitrogen Ligation Buffer, 0.1% Triton-X-100 (Sigma, 93443-500mL), and 0.01mg/mL BSA (Sigma Aldrich, A7906-50G). Ligated chromatin was then treated with 2x 50ug Proteinase K (ThermoFisher, 25530031) at 65 degrees C overnight to remove all cross-linked proteins, as in the published Hi-C 2.0/MC-3C protocols [27,44]. Ligation products

were purified by phenol:chloroform extraction with ethanol precipitation, as in Hi-C 2.0/MC-3C [27,44], with a final elution in 20ul $dH_2O$.

**PacBio Library Preparation**

Barcoded PacBio SMRTbell libraries for MC-3C replicate 1 of the mitotic release experiment were constructed by the UMass Chan Medical School PacBio Core Enterprise. All other MC-3C PacBio libraries were constructed using the following protocol. Barcoded PacBio SMRTBell adapters from the PacBio 8A barcoded adapter kit (Barcoded Overhang Adapter Kit - 8A, PacBio PN: 101-628-400) were added to ligation products following an adapted version of the PacBio Microbial Multiplexing PacBio protocol (Part Number 101-696-100 Version 07 (July 2020) ) using the PacBio SMRTbell Express Template Prep Kit 2.0 (PacBio, PN: 100-938-900) as follows: the ligated DNA was quantified using a Qubit fluorometer and Qubit HS DNA reagents, as recommended by the manufacturer (ThermoFisher, Q32851). DNA quantification was adjusted to 33ng/ul with 1x PacBio Elution Buffer (PacBio, PN: 101-708-100). Then 14.6ul of each ligated DNA sample was aliquoted into a 1.5ml DNA lo-bind tube (Eppendorf, Z666548). All reagents and master mixes were kept on ice throughout this protocol. To remove single-strand overhangs, DNA prep additive was first diluted 1:5 in enzyme dilution buffer. Next, the DNA prep master mix was added. For an 8-plex reaction, volumes including 25% overage for this mix were: 23.3ul DNA prep buffer, 3.3ul NAD, 3.3ul Diluted DNA Prep Additive, 3.3ul DNA Prep Enzyme. For each sample, 3.3ul of the DNA prep master mix were added to 14.6ul ligated DNA. Tubes were mixed by finger-tapping and briefly spun down, then incubated at 37 degrees C for 15 minutes.

Reactions were then returned to 4 degrees C. Next, the DNA Damage Repair master mix was prepared. For an 8-plex reaction, 6.7ul of DNA Damage Repair Mix v2 + 3.3ul Enzyme Dilution Buffer were added. Then 1.0ul of DNA Damage MM was added to each 17.9ul single strand digested sample. Tubes were mixed by finger-tapping and briefly spun down, then incubated at 37 degrees C for 30 minutes and returned to ice. End-Repair/A-tailing was performed in one step by adding 1ul of End Prep Mix to each 18.9ul damage-repaired sample. Tubes were finger-tapped to mix, briefly spun down, and incubated at 20 degrees C for 10 minutes, followed by 65 degrees C for 30 minutes, then returned to 4 degrees C. For ligation of barcoded overhang SMRTBell adapters, 2.0ul of adapters were added to each A-tailed sample first before adding ligase. Tubes were finger-tapped to mix and briefly spun down, then were placed on ice while the Ligation Master Mix was prepared. For an 8-plex reaction, the Ligation Master Mix contained 88ul Ligation Mix, 2.9ul Ligation Additive, and 2.9ul Ligation Enhancer. 10.7ul of ligation master mix was added to each A-tailed/Barcoded Adapter mix, followed by finger-tapping to mix, and a brief spin. Samples were incubated at 20 degrees C for 60 minutes, and then the ligase was heat killed by incubating at 65 degrees C for 10 minutes. SMRTBell libraries were then purified using 0.45X AMPure PB Beads, either 1 or 2 times. For 0.45X AMPure PB purification, AMPure PB beads were first brought to room temperature. Next, the volume of each library was adjusted to 100ul with PacBio Elution Buffer, and 45ul of the AMPure PB beads (0.45X volume) was added. Bead/DNA solution was mixed by gently tapping the tube, followed by a quick spin down to collect the beads. Mix was incubated at room temp for 5 minutes, quickly spun down, and placed on a magnetic bead rack for 5 minutes to collect the

beads to the side of the tube. Once supernatant was cleared, it was slowly pipetted off and discarded. Library DNA was now bound to beads. Beads were washed 2x with 80% ethanol without removing tubes from magnet by slowly pipetting 1ml into each tube, incubating for 30 seconds, and then slowly pipetting out the ethanol. Residual ethanol was removed by quickly spinning the tubes and returning to the magnetic tube rack. Any residual 80% ethanol droplets were pipetted off of the beads. For the first AMPure purification, DNA was eluted in 100ul 1x PacBio Elution buffer, while for the second purification DNA was eluted in 20ul Elution Buffer. To elute DNA, elution buffer was added to the tube and tube was mixed by finger-tapping to resuspend beads. Mix was incubated at 37 degrees for 15 minutes, then quick spun and placed on the magnetic bead rack until supernatant was clear. Supernatant containing DNA library was transferred to a new 1.5ml DNA Lo-Bind tube using a wide-bore lo-bind tip for the 100ul eluate, and a 20ul regular bore tip for the 20ul eluate, and beads were discarded. DNA quantity was measured using a Qubit fluorometer and the Qubit HS DNA kit. Libraries were analyzed by fragment analyzer to determine average size, and were sequenced on a PacBio Sequel II, using v8.0.0 (replicates 1 and 2) or v10.1.0 (replicate 3) instrument control software.

**MC-3C Analysis**

*CCS calling, demultiplexing, fastq extraction*

For replicates 1 and 2, PacBio SMRTTools version 8.0.0 was used for consensus consensus sequence (CCS) calling, demultiplexing, and fastq extraction. For replicate 3, PacBio SMRTTools version 10.1.0 was used for these analysis steps.

*Mapping and Annotation*

Reads in fastq format were mapped to the hg38 genome assembly downloaded from ENCODE (GRCh38_no_alt_analysis_set_GCA_000001405.15.fasta.gz) using minimap2 (v2.17) with the option *--secondary=no* [127,128]. Mapped C-walks were then annotated both at the fragment and the C-walk level for further filtering and analysis, including number of fragments per C-walk, number of chromosomes and compartment types visited, proximity of each fragment to the largest step in each C-walk, the size of the largest step for each C-walk, the distance of each direct pairwise interaction, the total span of each C-walk, and other features (see examples of custom python scripts used for mapping and secondary analysis on Github for further details). Fastq files containing CCS reads and tables of annotated C-walks are included on GEO.

*QC*

Mapped and annotated reads were filtered to include only reads where all fragments had a mapping quality >59, visited <3 chromosomes, were in regions of the genome called as A or B compartments by Hi-C, and >80% of the entire read was aligned to the genome. For the HeLa S3 libraries, only the chromosomes that have been determined to be minimally translocated were analyzed, as for the Hi-C experiments (chr4, chr14, chr1, chr18, chr20, chr21) [48]. In addition, except when analyzing raw read length and fragment number for each library, all analyses were performed on the first 6 fragments of all C-walks >= 6 fragments. To ascertain the quality of the data we compared MC-3C data to our Hi-C results. We considered C-walks visiting only one or two chromosomes and calculated the fraction of these C-walks within each compartment type (A, B, or A+B) (Figure 4B). All compartment regions were assigned based on compartment calls

from Hi-C data obtained with late G1 control (DMSO treated) cells, as shown in Figure 1, binned at 100kb resolution. In line with our Hi-C results, we found that prometaphase C-walks were more likely to be within one chromosome than between two chromosomes. In addition, we found that prometaphase C-walks were more likely to occur between A and B compartments as compared to interphase C-walks, consistent with mitotic chromosomes not being compartmentalized, as detected by Hi-C (Figure 4B, Figure S2D,O) [48]. As cells progress from mitosis into G1, more interchromosomal C-walks were detected, particularly those that involve interactions between two A compartments. Within chromosomes, the control cells increased the fraction of C-walks within only one type of compartment, while C-walks that occur between A and B compartments decreased as G1 progressed. In the presence of ICRF-193 the same trends were generally observed, except that the disappearance of C-walks between A and B compartments was slower (Figure 4B, compare $t$ = 4 hrs DMSO vs $t$ = 4 hrs ICRF-193, (1, AB)). ICRF-193 also delays the formation of interchromosomal C-walks. From these analyses, we conclude that MC-3C qualitatively recapitulates the main features observed in our Hi-C data.

*Descriptive plots*

Density plots of C-walk span, direct pairwise interaction distance, and read length were made using the kdeplot function from the python package seaborn (v0.11.2) [122]. Step style density plot of fragment number per read was made using python package seaborn (v0.11.2) [122]. Stacked barplots of C-walk type by chromosome number and compartment identity were made using DataFrame.plot function from the python package pandas (v1.4.2) [116].

*Intermingling Metric Analysis*

The Intermingling Metric (IM) was calculated using custom python scripts on either real or permuted C-walks. Permuted C-walks were made by shuffling the order of the first 6 fragments of C-walks >= 6 fragments 100 times for each library. To calculate intermingling, a sliding window algorithm was used on C-walks which interacted with only two regions on a single chromosome, as defined by all fragments being within ½ of the size of the largest step from either side of the largest step in the C-walk. C-walks were further filtered to only include C-walks where 5 fragments were close to side 1 of the largest step, and 1 fragment was close to side 2 of the largest step, allowing for either 1 or 2 steps between the two sides. The IM was calculated by binning C-walks with similar sizes of largest steps together depending on the window size (4Mb-16Mb, every 2 Mb), and calculating the fraction of C-walks within each window with 2 steps between the two sides of the largest step out of the total number of this type of C-walk. The window was then slid by 1Mb steps to 30Mb separation total (mitotic release experiment) or 50Mb total (cohesin degron experiment). The IM was plotted either as a heatmap organized by distance of separation on the *x* axis and window size on the *y* axis for each separate sample or for the log2 fold change between pairwise comparisons of samples. In addition, we used seaborn relplot to display the IM within selected window sizes (4Mb and 12Mb) as line plots for each pair of treatments showing the average IM (solid line) and the 95% CI of 3 biological replicates (surrounding shaded area), along with the average IM from permuted walks (3 replicates x 100 permutations each) (dashed line) with the 95% CI from all 300 permutations (surrounding shared area) [122]. To ensure that the large steps between the interacting

domains result are true contacts and not random ligations, we analyzed *P(s)* plots for either all pair-wise interactions from these two region C-walks, or the largest step from each two region C-walk, and found that the *P(s)* plots for both types of interactions were similar, with both displaying distance dependent decay in frequency, indicating that the largest steps follow the expected contact frequency, and therefore are not random ligations (Figure S4M). Examples of custom python scripts used for MC-3C analysis and visualization will be available on github.

**Immunofluorescence Microscopy Antibody Staining**

IF samples were prepared using standard methods. HeLa S3 or HeLa S3 + TOP2A-Venus cell linescells were either grown or spun onto 22x22mm No 1.5 coverslips in 6-well plates (VWR Cat No 48366-277). (cell cycle analysis experiments, euchromatin and heterochromatin localization experiments) or were spun onto 25x75x1.0mm Superfrost Plus Precleaned Microscope Slides with 13mm Single Rings (Fisher Cat No. 22-037-241) using a Cytospin 4 centrifuge (DNA and Topo II$\alpha$-Venus contrast experiments) (800rpm, 5min). For experiments with cells on coverslips, for adherent cells, the media was removed, cells were washed with DPBS (Gibco, 14190144), and were fixed in 4% Paraformaldehyde (Fisher, 15710) in 1x PBS (Gibco, 70013-073) for 10 minutes at room temp onto 22x22mm coverslips in a 6-well plate, and were then washed 3x with 1x PBS before proceeding to staining. For suspension cells, an equal volume of the cell suspension in media and 8% paraformaldehyde in 1x PBS was mixed together and added to a 6-well plate containing a 22x22mm coverslip. The plate was then centrifuged for 15 min at 800xg, during which time the cells were fixed and became

adhered to the coverslip, and were then washed 3x with 1x PBS before proceeding to staining. For experiments using the Cytospin 4, for adherent cells the media was first collected, and cells were washed 1x with DPBS before cells were disassociated with TrypLE Express (ThermoFisher, 12605036), and combined with the collected media. For suspension cells, the cell suspension was collected directly. Cell suspensions were spun to pellet cells, and were washed 1x with 1x PBS, and then fixed for 10 minutes in 4% Paraformaldehyde at room temp. After fixation, cells were washed 1x with PBS, then resuspended in 1ml PBS and stored at 4 degrees C in dark. 0.5-1.5x10^5 fixed cells were spun onto slides using the Cytospin 4, using Shandon™ EZ Single Cytofunnel™ with White Filter Cards and Caps (Thermo Fisher, A78710020). After removal of the Cytofunnel, cells were allowed to dry for a few minutes, before proceeding to staining. To stain cells , slides or coverslips were first incubated in block buffer (3% BSA (Sigma Aldrich, A7906-50G), 0.1% Triton-X-100 (Sigma, 93443-500mL), 1x PBS) in a humidified chamber for 30 minutes to 2 hours at room temp, or overnight at 4 degrees C. To prevent evaporation, droplets of buffer on cells were covered with squares of parafilm during incubation. After blocking, primary antibody in block buffer was added to each slide or coverslip, which was incubated for 2 hours at room temp or overnight at 4 degrees C. Slides or coverslipsCoverslips were washed 3x 5 min in 1x PBS + 0.1% Triton-X-100 after primary antibody incubation in a , either in Coplin jars (slides), or in 6 well plate (cover slips). Secondary antibody in block buffer was added next and incubated for 30 minutes at room temp, in a dark humidified chamber. Slides or coverslips were then washed 3x5min in 1x PBS + 0.1% Triton-X-100, and then 2x in PBS without detergent. For DAPI stained coverslips or slides, this

was followed either by a 10min incubation at room temp with 3uM DAPI in PBS (Invitrogen, D1306), or by using ProLong Diamond mounting media containing DAPI (Invitrogen, P36962). Before mounting, slides or coverslips were washed 5min in distilled water and allowed to air dry, they were then mounted using ProLong Diamond mounting media either with DAPI (Invitrogen, P36962) or without DAPI (Invitrogen, P36961), and allowed to cure for at least 24 hours in the dark before imaging. Primary antibodies used: rabbit anti-Lamin A (Abcam ab26300, 1:1000 dilution), rabbit anti-H3K9me3 (Abcam ab8898, 1:500 dilution), mouse anti-H3K27ac (Active Motif 39085, 1:500 dilution), mouse anti-Alpha Tubulin (Sigma T6199, 1:5000 dilution). Secondary antibodies used: goat anti-mouse IgG H+L Alexa Fluor 568 (1:1,000, Abcam ab175473), goat anti-rabbit IgG H&L Alexa Fluor 488 (1:1,000, Abcam ab15007)

**Widefield Fluorescence Microscopy**

For widefield fluorescent image acquisition, we used a Nikon Eclipse Ti microscope. Imaging was performed using an Apo TIRF, N.A. 1.49, 60x oil immersion objective (Nikon), and a Zyla sCMOS camera (Andor). Images were acquired using Nikon Elements software (Version 4.4). Data are available in the BioStudies database (https://www.ebi.ac.uk/biostudies/) [129].

**Confocal Fluorescence Microscopy**

For image acquisition, we used a Nikon A1 point-scanning confocal microscope with 405 nm, 488 nm and 561 nm lasers. Imaging was performed using an Apo TIRF, N.A. 1.49, 60x oil immersion objective (Nikon) with GaAsP detectors (488 and 561 lasers) or

a high sensitivity MultiAlkali PMT (405 laser) at 0.1um/pixel resolution, resulting in 512/512 pixel images, in Galvano imaging mode. Z-steps were 1um for images taken as Z-series. Images were acquired using Nikon Elements software (Version 4.4). Data are available in the BioStudies database (https://www.ebi.ac.uk/biostudies/) [129].

**Microscopy Analysis**

*Cell Cycle Staging*

Cell cycle stage of wide-field immunofluorescence images was analyzed by blinding the images and manually classifying each cell into a cell cycle category based on morphological features using Nikon Elements software.

*Euchromatin and Heterochromatin Localization*

Confocal images of H3K27ac and H3K9me3 localization were analyzed using CellProfiler v4.1.3. For each Z-slice, images were first segmented using the DAPI signal to identify nuclei, with object tracking to link nuclei between Z-slices for each image based on location. Next, H3K9me3 and H3K27ac objects were identified within each Z-slice for each nucleus. To avoid out of focus images, and to obtain one representative cross-section of each nucleus, one Z-slice per nucleus was considered for further analysis, which was selected by having the largest nuclear area, H3K9me3 and H3K27ac object counts between the 20% and 90% quantiles within each experiment, nuclear compactness < 90% quantile, and area solidity > 10% quantile. Within this representative Z-slice, the % of H3K27ac objects containing H3K9me3 objects, the radial distribution of each signal in 10 radial bins within each nucleus, and the number and average area of H3K9me3 objects per nucleus were calculated.

*Texture Analysis*

Single Z-slice confocal images from approximately the center of each nucleus were analyzed for DNA and TOP2A-Venus signal contrast using CellProfiler (v4.1.3) to segment nuclei using DAPI signal, and save all channels for each nucleus separately [130]. These images were then used to calculate Haralick features using the python library mahotas (v1.4.11) [64]. Contrast at a distance of 10 pixels (1um) averaged across all 4 directions for each nucleus was used to compare the textures of DNA (DAPI) and TOP2A-Venus between samples. Statistical analysis was performed using 2-way ANOVA in Graphpad Prism. CellProfiler Pipelines and python code used for image analysis are available in the BioStudies database (https://www.ebi.ac.uk/biostudies/) [129].

**Western Blots**

Protein immunoblots were performed using standard methods. Protein lysates were made by harvesting the same number of cells (generally 0.5x10^6 each) for each sample in an experiment and lysing in 2x Laemmli Buffer (.07M Tris pH6.8, 10% sucrose, 3% SDS, 50mM DTT) by boiling for 10 minutes. Western blots were performed by running protein lysates on 4-12% NuPage Bis-Tris gels using 1x MES running buffer for 45 minutes at 175V using an Invitrogen XCell Sure-Lock minigel and blotting system. Gels were transferred to 0.2um nitrocellulose membrane in Pierce™ 10X Western Blot Transfer Buffer, Methanol-free (Thermo Fisher Scientific, 35040), by running for 1 hour at 30V at 4 degrees C. The membranes were blocked with 4% milk in PBS-T (1x PBS and 0.1% Tween-20) for 30 minutes at room temperature. The membranes were then incubated with the specified antibodies diluted in 4% milk/PBS-T either for 2 hours at

room temp or overnight at 4 degrees C, and washed three times with PBS-T for 10 minutes at room temperature. Membranes were then incubated with secondary antibodies (anti-rabbit IgG or anti-mouse IgG HRP linked) diluted 1:4000 in 4% milk/PBS-T for 30 minutes to 1 hr at room temperature, then washed three times with PBS-T for 10 minutes at room temperature. The membranes were then developed and imaged using SuperSignal West Dura Extended Duration Substrate (Thermo, 34076) and a Bio-Rad ChemiDoc. Primary antibodies used: mouse anti-Topoisomerase IIα (1:500, Santa Cruz sc-166934), rabbit anti-DNA Topoisomerase IIα and DNA Topoisomerase IIβ (1:10,000, Abcam ab109524), rabbit anti-GFP (1:5,000, abcam ab290), mouse anti-β-actin (1:2,000, Cell Signaling 8H10D10), mouse anti-cyclin B1 (1:500, Cell Signaling 4135), rabbit anti GAPDH (1:1000, Cell Signaling 14C10). Secondary antibodies used: goat anti-rabbit IgG-HRP (1:4,000, Cell Signaling 7074), goat anti-mouse IgG-HRP (1:4,000, Cell Signaling 7076).

**Details of polymer modeling**

*Simulations setup*

Polymer simulations were performed using polychrom (available at https://github.com/open2c/polychrom), a wrapper around the open source GPU-assisted molecular dynamics package OpenMM [131]. We simulated a chain of the length $N \approx 22500$ monomers, each monomer representing 4kb chromatin bead (90Mb in total). To emulate the interactions with other chromosomes, simulations were conducted in periodic boundary conditions and with an interphase volume density $\rho\sigma^3 \approx 0.2$, where $\sigma$ is the length scale of excluded volume interactions (see below).

The chains were equipped with harmonic bonds $U_{bond}$ and excluded volume interactions. The energy of harmonic bonds reads as follows

$$U_{bond} = \frac{3}{2a^2}\sum_{i=1}^{N-1}\left(r_{i,i+1} - l_b\right)^2,$$

where $a$ is the standard deviation of the monomer-to-monomer spatial distance $r_{i,i+1} = |r_i - r_{i+1}|$ from the equilibrium bonds length $l_b$. Note that, by default, one defines the "wiggle distance" in polychrom, which is $\sqrt{3/2}$ times smaller. The excluded volume potential $U_{ev}$ is introduced through the auxiliary Weeks-Chandler-Anderson (WCA) potential $U_{WCA}(r_i, r_j)$, which is a lifted repulsive branch of the Lennard-Jones potential

$$U_{WCA}(r_i, r_j) = U_{WCA}(r_{ij}) = \begin{cases} 4\varepsilon\left(\left(\frac{\sigma}{r_{ij}}\right)^{12} - \left(\frac{\sigma}{r_{ij}}\right)^{6}\right) + \varepsilon, & r_{ij} \le 2^{1/6}\sigma \\ 0, & r_{ij} > 2^{1/6}\sigma \end{cases}$$

where $\sigma$ is the characteristic length scale of excluded volume interactions, at which $U_{WCA}$ equals to $\varepsilon = 1kT$. In order to avoid singularities of the excluded volume potential (infinite forces), the WCA potential is further smoothly truncated at zero as follows

$$U_{ev}(r_{ij}) = H\left(U_{WCA}(r_{ij}) - \varepsilon_{tr}\right)\varepsilon_{tr}\left(1 + \tanh\left(\frac{U_{WCA}(r_{ij})}{\varepsilon_{tr}} - 1\right)\right)$$
$$+ H\left(\varepsilon_{tr} - U_{WCA}(r_{ij})\right)U_{WCA}(r_{ij})$$

at the prescribed truncation value $\varepsilon_{tr}$; $H(x)$ is the Heaviside step function. The excluded volume potential was further switched off for the neighboring monomers in the chain.

In order to model the reduced Topo II activity (in the second stage of the two-stage mechanism), we introduce (i) a tunable excluded volume repulsion between the chain beads by setting $\varepsilon_{tr} = 3, 5$ or $10kT$, which is sufficient to achieve strong mutual volume

exclusion of the beads, and (ii) short polymer bonds with $l_b = 0.6\sigma$, which was chosen phenomenologically to ensure prohibition of strand passage. To that end, separate simulations of a mitotic chromosome were performed, where conservation of topology was controlled by the matrices of pairwise linking numbers between the mitotic (condensin) loops, which were invariant in the course of simulation. Notably, for $l_b = \sigma$ some occasional strand passage can occur, despite of the high excluded volume barrier, thus, a lower value of the equilibrium bond length was chosen. On contrary, in simulations of high activity of Topo II the excluded volume barrier was decreased to $\varepsilon_{tr} = 1kT$, while the bond length was kept $l_b = 0.6\sigma$ in order not to change the volume density. Under such a low excluded volume barrier loops become mutually catenated, as the chain gets effectively phantom.

*Initial state*

For each of the replicates the simulations of mitotic exit were initiated with a chromosome folded into a sequence of 225 random loops, exponentially distributed in size with the mean $\lambda \approx 400$ kb (except for the last one, for which the size was chosen such that the lengths of all the loops sum up to $N$). This chain was further constrained within a cylindrical volume with the longitudinal length $L = 50\sigma$ and the radius $R = 14\sigma$, such that the volume density of the mitotic chromosome was equal to $\rho_{init}\sigma^3 \approx 0.45$. Similarly to [50], in order to obtain spiralization of the backbone, we equidistantly tethered each 20$^{th}$ loop at the axis of the cylinder, as well as the ends of the chain were tethered to the caps of the cylinder at the axis. This tethering was found to be important to screen out large-scale contacts in the chain.

In order to prepare an initial state with mutually non-catenated loops we performed slow extrusion of the loops with sizes sampled from the exponential distribution, under inhibited strand passage conditions (high excluded volume barrier), following by equilibration of the mitotic structure As the matrix of linking numbers between the loops shows (Figure 5A), this results in array of mutually non-catenated loops on the chain. An initial state with catenated loops was obtained from the non-catenated mitotic state by decreasing the barrier on excluded volume to $\varepsilon_{tr} = 1kT$ (emulating high activity of Topo II) and a round of axial compression of the chromosome to the density $\rho_{init}\sigma^3 \approx 0.6$ and restoring its longitudinal size back to $L = 50\sigma$. Eventually, the mean number of catenations per one loop in the catenated mitotic state was close to $\approx 0.7$ (see Figure 5A), thus, ~66% of the loops are catenated at least once with another one. The mean genomic distance between the catenated loops in this state was equal to ~9Mb (~22 loops), corresponding to the size of the mitotic layer.

*Compartments and TADs in the second stage*

During the second stage of mitotic exit we add compartmental interactions, giving rise to compartments, and active loop extrusion, resulting in topologically-associated domains on the simulated Hi-C maps. Namely, the two features are added to the simulation at the same moment when condensin loops are released from the chain, i.e. after a certain duration $T$ of the first stage (in both, strand passage inhibited and wild type simulations).

For compartmental interactions we use the experimental annotation into the compartments. For that, we used the first eigenvector of the centralized observed over expected Hi-C map (Late G1 DMSO combined R1 + R2 sample, see Hi-C Compartment Analysis methods section for details) for chromosome 14 in the 250kb resolution. The first 20Mb segment of the chromosome consists of NaN values and, thus, it was eliminated from the analysis. The remaining part of the eigenvector was used to assign the compartmental types: positive components corresponded to the type A, negative and zero components corresponded to the type B (each component of the eigenvector generated a batch of 63 4kb-monomers of the same type). To comply with the smoothed and truncated excluded volume potential, used for interactions of the beads of different type, we introduced the following attractive potential between the beads of the same type

$$U_{same}(r_{ij}) = H\left(r_{ij} - \sigma_{rep}\right)U_{attr}(r_{ij})$$

where $\sigma_{rep} = 2^{1/6}\sigma$ is the scale, above which there is no repulsion between the beads, and attraction of the same-type-beads is turned on according to the potential

$$U_{attr}\left(r_{ij}\right) = -\varepsilon_{attr}\left(\Delta r_{ij}^{12}\left(\Delta r_{ij}^{2} - 1\right)e_0 + 1\right)$$

where $e_0 = 823543.0/46656.0$ is some constant and $\Delta r_{ij}$ is the scaled distance

$$\Delta r_{ij} = \frac{r_{ij} - \sigma_{rep} - \Delta_{attr}}{\Delta_{attr}} r_0,\ \Delta_{attr} = \frac{\sigma_{attr} - \sigma_{rep}}{2}, r_0 = \sqrt{6/7}$$

The special choice of constants $e_0$ and $r_0$ ensured that the potential smoothly goes to zero at $\sigma_{rep}$ and $\sigma_{attr}$ and has an attractive valley in between these two length scales at $\varepsilon_{attr}$. For all simulations we used parameters $\varepsilon_{attr} = 0.07kT$ and $\sigma_{attr} = 1.5\sigma$, which resulted in relatively weak micro-phase separation corresponding to experimental Hi-C compartmental scores [132].

Active loop extrusion was simulated in two steps: one-dimensional extrusion process followed by incorporation of the loops into the three-dimensional polymer simulation. For the one-dimensional loop extrusion we preset the positions of the TAD boundaries at the positions inferred by calling insulation minima on the Late G1 DMSO R1 + R2 combined experimental Hi-C matrix for chromosome 14 (see Hi-C Insulation Profiles methods section for details). Then extrusion between the boundaries was performed with permeability of the TAD boundary (probability for extruder to bypass the boundary) $p \approx 0.1$, with the resulting average loop size $\lambda \approx 160$ kb and the average gap size $g \approx 160$ kb, corresponding to ≈ 50% coverage of the chain by loops. Cohesin motors were simulated as stochastically exchanging with the chain; loops were linearly growing with time while the cohesins were bound (unless blocked by the boundaries), with respect to the boundaries. In the three-dimensional simulation the sampled configurations of loops for each replicate, starting from the very beginning of extrusion, were put as harmonic constraints with the same energy as the polymer bonds. The configuration of loops was renewed every 4 seconds of a three-dimensional polymer simulation, resulting in extrusion rate of $r = 1$ kb/s, typical for cohesin *in vitro* [133-135]. The chosen parameters resulted in generation of TADs on the averaged (over 8 replicates and time) contact maps at the positions preset by the experimental boundaries, and were similar to TADs observed on experimental Hi-C maps.

*Calibration of timescales in simulations*

The timescales in simulations were calibrated to match the experimental timescales. For that, we have computed the mean-squared displacements (MSD) of the monomers $\langle R_n^2(t)\rangle$, averaged over different monomers in the chain, as a function of time. The MSDs were measured in separate short-time simulations starting from the expanded state (late interphase; the end of the second stage of the two-stage process). As expected, at times larger than the diffusion time between the neighboring Kuhn segments, the MSD follows the Rouse diffusion, $\langle R_n^2(t)\rangle = Dt^{0.5}$, with a smooth crossover to $\langle R_n^2(t)\rangle \sim t^{0.4}$ at larger times, which is behavior of topologically-constrained "crumpled" chains in the generalized Rouse model for the fractal dimension of the chain $d_f \approx 3$ [71,136,137].

The conversion of times between simulations and experiments was performed by matching the values of the Rouse diffusion coefficient, $D$. Every block of steps in the simulations corresponded to 1 sec, which resulted in the value of $D \approx 0.035\ \mu^2/s^{1/2}$. The monomer size is assumed to equal $\sigma = 30\ nm$ for this calculation. The experimental values of the diffusion coefficient vary between the organisms and experiments, however, the used value in simulation is consistent with the experiments up to the order of magnitude. The used conversion scale further matches observation of the Rouse diffusion in locus tracking experiments starting from sub-seconds time.

As an independent way of calibration of timescales, we estimate the characteristic mitotic exit time as the time needed to reach the topological steady state during the first stage of the two-stage model. Namely, we observe that in $T = 1 - 2$ hours the mitotic chain is decompacted under high activity of Topo II to the state with stationary amount

of catenated loops and stationary territoriality (Fig. 6). This time matches the transition time from mitosis to the early interphase as was observed in [47].

**FIGURE LEGENDS:**

**Figure 1: Topo II inhibition by ICRF-193 delays compartment re-establishment at G1 entry**

A. Schematic of Topo II inhibition by ICRF-193 treatment in asynchronous (AS) HeLa S3 cells with G1 sorting. Cells were treated for two hours with DMSO or 30uM ICRF-193, and then fixed for Hi-C with 1% formaldehyde (FA). G1 cells were sorted using propidium iodide (PI) staining for DNA content. G1 sorted cells were analyzed by Hi-C 2.0 with DpnII digestion.

B. Flow cytometry profiles of DNA content (PI stain) of AS HeLa S3 cells with two-hour DMSO or 30uM ICRF-193 treatment before sorting.

C. Hi-C interaction heatmaps of AS G1 sorted HeLa S3 cells treated with DMSO or 30uM ICRF-193, for the q arm of Chr14. Binned at 250kb with iterative correction and read normalized between samples, two replicates combined. Eigenvector 1 is plotted below each heatmap.

D. Hi-C interaction log10 ratio heatmap comparing ICRF-193 treatment to DMSO control AS samples. Binned at 250kb with iterative correction and read normalized between samples, two replicates combined.

E. Schematic of HeLa S3 mitotic synchronization and release experiment with Topo II inhibition by ICRF-193 treatment. HeLa S3 cells were synchronized in S phase by 24hr treatment with 2mM Thymidine, released three hours, then arrested in prometaphase

with a 12hr treatment with nocodazole. Prometaphase cells (*t* = 0) were collected by mitotic shake-off, washed, and released into fresh media. DMSO or 30uM ICRF-193 was added *t* = 2 hrs post mitotic release (MR). Cells were incubated a further two (early G1, *t* = 4 hr timepoint) or six (late G1, *t* = 8 hr timepoint) hours, before fixation for Hi-C with 1% FA. G1 cells were sorted using propidium iodide (PI) staining for DNA content. G1 sorted cells were analyzed by Hi-C with DpnII digestion.

F. Flow cytometry profiles of DNA content (PI stain) of cells described in E. before G1 sorting.

G. Hi-C interaction heatmaps of G1 sorted MR HeLa S3 cells treated with DMSO or 30uM ICRF-193, for the q arm of Chr14. Binned at 250kb with iterative correction and read normalized between samples, two replicates combined. Eigenvector 1 is plotted below each heatmap.

H. Hi-C interaction log10 ratio heatmap comparing ICRF-193 treatment to DMSO control for each timepoint. Binned at 250kb with iterative correction and read normalized between samples, two replicates combined

I. *P(s)* scaling plot of G1 sorted HeLa S3 cells (AS and MR from separate experiments, as above), treated with DMSO or 30uM ICRF-193. AS DMSO (light blue), AS ICRF-193 (pink), MR 4hrs early G1 DMSO (bright blue), MR 4hrs early G1 ICRF-193 (bright red), MR 8hrs late G1 DMSO (dark blue), MR 8hrs late G1 ICRF-193 (dark red). Two replicates combined. Prometaphase *P(s)* plot from a single replicate of a separate experiment (heatmap shown in Figure S2D) is shown as dotted grey line for comparison.

J. First derivative (slope) of *P(s)* scaling plot shown in I. (AS and MR from separate experiments, as above)

K. AA compartment strength log2 ratio compared to control at each collection time by distance, for G1 sorted HeLa S3 cells, AS DMSO/AS ICRF-193 (grey), MR 8hrs late G1 DMSO/MR 4hrs early G1 DMSO (light blue), MR 4hrs early G1 ICRF-193/MR 4hrs early G1 DMSO (bright red), MR 8hrs late G1 ICRF-193/MR 8hrs late G1 DMSO (dark red). N=2 for each sample. 250kb binned data. Bar graph shows mean of two biological replicates, scatterplot overlay shows values from individual replicates. (AS and MR from separate experiments, as above)

L. BB compartment strength log2 ratio compared to control at each collection time by distance, for G1 sorted HeLa S3 cells, AS DMSO/AS ICRF-193 (grey), MR 8hrs late G1 DMSO/MR 4hrs early G1 DMSO (light blue), MR 4hrs early G1 ICRF-193/MR 4hrs early G1 DMSO (bright red), MR 8hrs late G1 ICRF-193/MR 8hrs late G1 DMSO (dark red). N=2 for each sample. 250kb binned data. Bar graph shows mean of two biological replicates, scatterplot overlay shows values from individual replicates. (AS and MR from separate experiments, as above)

M. Representative confocal microscopy images of DAPI (DNA), H3K9me3 (green, heterochromatin), and H3K27ac (red, euchromatin), in Early ($t$ = 4 hrs) and Late ($t$ = 8 hrs) G1 HeLa S3 cells after mitotic release with either DMSO or 30uM ICRF-193 treatment from $t$ = 2 hrs post nocodazole washout. One Z-slice near the center of each nucleus was analyzed and is shown. Top is merge of all channels, autoscaled within each channel of each image to the maximum dynamic range. Bottom is the same merged image with an overlay (white lines) of the H3K27ac segmented objects

containing H3K9me3 objects, as used for quantification of overlap between the two types of chromatin in N.

N. Quantification of the confocal microscopy experiment shown in M, boxplot of the fraction of H3K27ac segmented regions that contain H3K9me3 segmented for each nucleus. q-values shown on graph from 2-way ANOVA analysis with multiple comparison correction using false discovery rate (FDR = 0.05) using the method of two-stage linear step-up procedure of Benjamini, Krieger and Yekutieli with one family per experimental replicate. Boxplot shows min, 25%, 50%, 75%, max. Scatterplot overlay shows individual values for each nucleus. Samples: MR 4hrs early G1 DMSO (bright blue), MR 4hrs early G1 ICRF-193 (bright red), MR 8hrs late G1 DMSO (dark blue), MR 8hrs late G1 ICRF-193 (dark red)

O. Quantification of the confocal microscopy experiment shown in M. Boxplot of the mean fraction of H3K27ac signal in the outermost (peripheral) radial bin, out of 10 total bins. q-values shown on graph from 2-way ANOVA analysis with multiple comparison correction using false discovery rate (FDR = 0.05) using the method of two-stage linear step-up procedure of Benjamini, Krieger and Yekutieli with one family per experimental replicate. Boxplot shows min, 25%, 50%, 75%, max. Scatterplot overlay shows individual values for each nucleus. Samples: MR 4hrs early G1 DMSO (bright blue), MR 4hrs early G1 ICRF-193 (bright red), MR 8hrs late G1 DMSO (dark blue), MR 8hrs late G1 ICRF-193 (dark red)

**Figure 2: Changes in supercoiling and transcription do not phenocopy Topo II inhibition by ICRF-193.**

A. Schematic of TOP1 inhibition by camptothecin (Camp.) treatment in AS HeLa S3 cells. Cells were treated for four hours with DMSO or 5uM camptothecin, then all adherent cells were fixed for Hi-C with 1% formaldehyde (FA). Hi-C was performed using the Hi-C 2.0 protocol with DpnII digestion.

B. Flow cytometry profiles for DNA content (PI stain) of AS HeLa S3 cells treated with DMSO or 5uM camptothecin for four hours, as described in A. Replicate one is shown in main figure, see Figure S2Y for replicate two cell cycle profiles.

C. Hi-C interaction heatmaps of unsorted HeLa S3 cells treated with DMSO or 5uM camptothecin during AS growth for four hours, for the q arm of Chr14. Binned at 250kb with iterative correction and read normalized between samples, two replicates combined. Eigenvector 1 is plotted below each heatmap.

D. Hi-C interaction log10 ratio heatmap comparing camptothecin treatment to DMSO control for AS cells, 250kb bins. Two replicates combined.

E. Schematic of HeLa S3 mitotic synchronization and release experiment with TOP1 inhibition by camptothecin treatment. HeLa S3 cells were synchronized in S phase by 24hr treatment with 2mM Thymidine, released three hours, then arrested in prometaphase with a 12hr treatment with nocodazole. Mitotic cells were collected by mitotic shake-off, washed, and released into fresh media containing DMSO or 5uM camptothecin. Cells were incubated a further six hours (late G1, $t$ = 6 hr timepoint) before fixation of adherent cells for Hi-C 2.0 with 1% FA. Chromosome structure was analyzed by Hi-C 2.0 with DpnII digestion.

F. Flow cytometry profiles for DNA content (PI stain) of cells described in E, replicate one shown in main figure, see Figure S2Z for replicate two.

G. Hi-C interaction heatmaps of unsorted HeLa S3 cells treated with DMSO or 5uM camptothecin during G1 entry (*t* = 6 hrs, late G1 timepoint), for the q arm of Chr14. Binned at 250kb with iterative correction and read normalized between samples, two replicates combined. Eigenvector 1 is plotted below each heatmap.

H. Hi-C interaction log10 ratio heatmap comparing camptothecin treatment to DMSO control during G1 entry (*t* = 6 hrs, late G1 timepoint), 250kb bins. Two replicates combined.

I. AA compartment strength log2 ratio compared to DMSO by distance, separated by compartment type, for HeLa S3 cells, AS Camp/AS DMSO (red), MR 6hrs late G1 Camp/MR 6hrs late G1 DMSO (gold). N=2. 250kb binned data. Bar graph shows mean of two biological replicates, scatterplot overlay shows values from individual replicates. AS and MR samples are from separate experiments.

J. BB compartment strength log2 ratio compared to DMSO by distance, separated by compartment type, for HeLa S3 cells, AS Camp/AS DMSO (red), MR 6hrs late G1 Camp/MR 6hrs late G1 DMSO (gold). N=2. 250kb binned data. Bar graph shows mean of two biological replicates, scatterplot overlay shows values from individual replicates. AS and MR samples are from separate experiments.

K. Schematic of HeLa S3 mitotic synchronization and release experiment with transcription inhibition and Topo II inhibition. HeLa S3 cells were synchronized in S phase by 24hr treatment with 2mM Thymidine, released 3 hours, then arrested in prometaphase with a 12hr treatment with nocodazole. Mitotic cells were collected by mitotic shake-off, washed, and released into fresh media containing either DMSO or DRB + Triptolide (Txn Inhib). 30uM ICRF-193 was added at *t* = 2 hrs after mitotic

release for the ICRF-193 only sample, and *t* = 2.5 hrs after mitotic release for the ICRF-193 + DRB + Triptolide (Txn Inhib) sample. Cells were incubated a further two hours (Early G1, *t* = 4 hrs timepoint for DMSO and ICRF-193 only, *t* = 4.5 hrs timepoint for Txn Inhib and Txn Inhib + ICRF-193 samples) before fixation of adherent cells for Hi-C 2.0 with 1% FA. Chromosome structure was analyzed by Hi-C 2.0 with DpnII digestion.

L. Flow cytometry profiles for DNA content (PI stain) of MR HeLa S3 cells treated with DRB +TRP (Txn Inhib) and/or ICRF-193 to inhibit Topo II, as described in K. Replicate one is shown in main figure, see Supp 2 for replicate two cell cycle profiles.

M. Hi-C interaction heatmaps of unsorted HeLa S3 cells treated with DMSO, ICRF-193, and/or DRB + TRP (Txn Inhib) at mitotic exit and collected for Hi-C in Early G1 (*t* = 4 hrs or *t* = 4.5 hrs), for the q arm of Chr14. Binned at 250kb with iterative correction and read normalized between samples, two replicates combined. Eigenvector 1 is plotted below each heatmap.

N. Percentage of cells in G1 over time during mitotic exit with DMSO or DRB + TRP (Txn Inhib) treatment from nocodazole wash-out. N = 1.

O. Hi-C interaction log10 ratio heatmap comparing ICRF-193, DRB + TRP (Txn Inhib), or the combination to DMSO control for each treatment type, 250kb bins. Two replicates combined.

P. AA compartment strength log2 ratio compared to DMSO by distance, separated by compartment type, for MR HeLa S3 cells. MR 4hrs early G1 ICRF-193/MR 4hrs early G1 DMSO (red), MR 4.5hrs early G1 Txn Inhib/MR 4hrs early G1 DMSO (purple), MR 4.5hrs early G1 ICRF-193 + Txn Inhib/MR 4hrs early G1 DMSO (gold). N=2. 250kb

binned data. Bar graph shows mean of two biological replicates, scatterplot overlay shows values from individual replicates.

Q. BB compartment strength log2 ratio compared to DMSO by distance, separated by compartment type, for MR HeLa S3 cells. MR 4hrs early G1 ICRF-193/MR 4hrs early G1 DMSO (red), MR 4.5hrs early G1 Txn Inhib/MR 4hrs early G1 DMSO (purple), MR 4.5hrs early G1 ICRF-193 + Txn Inhib/MR 4hrs early G1 DMSO (gold). N=2. 250kb binned data. Bar graph shows mean of two biological replicates, scatterplot overlay shows values from individual replicates.

**Figure 3: Topo II inhibition must occur during mitotic exit to delay compartment establishment**

A. Schematic of HeLa S3 mitotic synchronization and release experiment with ICRF-193 treatment starting at *t* = 2 hrs, collected at *t* = 4 hrs (early G1) or *t* = 8 hrs (late G1), without sorting. HeLa S3 cells were synchronized in S phase by 24hr treatment with 2mM Thymidine, released three hours, then arrested in prometaphase with a 12hr treatment with nocodazole. Mitotic cells were collected by mitotic shake-off, washed, and released into fresh media, or fixed with 1% FA for Hi-C 2.0 (floating cells only). DMSO or 30uM ICRF-193 was added *t* = 2 hrs after mitotic release. At this timepoint the *t* = 2 hrs (anaphase/telophase) cells were fixed with 1% FA for Hi-C 2.0 (floating + adherant cells). DMSO and ICRF-193 treated cells were incubated a further two hours (Early G1, *t* = 4 hrs timepoint) or six hours (Late G1, *t* = 8 hrs timepoint) before fixation of only adherent cells for Hi-C 2.0 with 1% FA. Chromosome structure was analyzed by Hi-C 2.0 with DpnII digestion.

B. Schematic of HeLa S3 mitotic synchronization and release experiment with ICRF-193 treatment starting at *t* = 2 hrs, re-added at *t* = 4 hrs and *t* = 6 hrs, collected at *t* = 8 hrs (late G1), without sorting. HeLa S3 cells were synchronized in S phase by 24hr treatment with 2mM Thymidine, released three hours, then arrested in prometaphase with a 12hr treatment with nocodazole. Mitotic cells were collected by mitotic shake-off, washed, and released into fresh media, or fixed with 1% FA for Hi-C 2.0 (floating cells only). DMSO or 30uM ICRF-193 was added at *t* = 2 hrs after mitotic release, and media was changed with fresh DMSO or 30uM ICRF-193 re-added every two hours (at *t* = 4 hrs and *t* = 6 hrs). Adherent cells were fixed after a total of six hours of treatment (Late G1, *t* = 8 hr timepoint) for Hi-C 2.0 with 1% FA. Chromosome structure was analyzed by Hi-C 2.0 with DpnII digestion.

C. Flow cytometry profiles for DNA content (PI stain) of synchronized HeLa S3 cells released into G1 with DMSO or 30uM ICRF-193 added at *t* = 2 hrs, collected in early G1 (*t* = 4 hrs), and late G1 (*t* = 8 hrs) with ICRF-193 added once at *t* = 2 hrs. Hi-C was performed on entire adherent cell population without G1 sorting. Replicate one plots for G1 timepoints shown in main figure. Plots for *t* = 0 (prometaphase) and *t* = 2 hrs (anaphase/telophase) replicate one, as well as all Replicate two plots are shown in Figure S3C,D.

D. Flow cytometry profiles for DNA content (PI stain) of synchronized HeLa S3 cells released into G1 with DMSO or 30uM ICRF-193 added at *t* = 2 hrs, collected in late G1 (*t* = 8 hrs) with ICRF-193 added added at *t* = 2 hrs and then re-added at *t* = 4 hrs and *t* = 6 hrs (Readded samples). Hi-C was performed on entire adherent cell population

without G1 sorting. Replicate one plots for shown in main figure. Replicate two and three plots are shown in Figure S3A,B.

E. Hi-C interaction heatmaps of unsorted HeLa S3 cells treated with DMSO, ICRF-193 at *t* = 2 hrs and collected at *t* = 4 hrs or *t* = 8 hrs, or DMSO or ICRF-193 added at *t* = 2 hrs, and readded at *t* = 4 hrs, and *t* = 6 hrs, and collected at *t* = 8 hrs, for the q arm of Chr14. Binned at 250kb with iterative correction and read normalized between samples, two replicates combined. Eigenvector 1 is plotted below each heatmap. With and without re-adding samples are from separate experiments.

F. Hi-C interaction log10 ratio heatmap comparing ICRF-193 treatment to DMSO control for each treatment type, 250kb bins. Two replicates combined. With and without re-adding samples are from separate experiments.

G. AA Hi-C compartment strength log2 ratio compared to DMSO by distance, separated by compartment type, for HeLa S3 cells. MR 4hrs early G1 ICRF-193/MR 4hrs early G1 DMSO (bright red) N=2, MR 8hrs late G1 ICRF-193 at *t* = 2 hrs/MR 8hrs late G1 DMSO at *t* = 2 hrs (dark red) N=2, MR 8hrs late G1 with ICRF-193 at *t* = 2 hrs with readding at *t* = 4 hrs and *t* = 6 hrs/MR 8hrs DMSO at *t* = 2 hrs with readding at *t* = 4 hrs and *t* = 6 hrs (beige). N=3. 250kb binned data. Bar graph shows mean of two biological replicates, scatterplot overlay shows values from individual replicates. With and without re-adding samples are from separate experiments.

H. BB Hi-C compartment strength log2 ratio compared to DMSO by distance, separated by compartment type, for HeLa S3 cells. MR 4hrs early G1 ICRF-193/MR 4hrs early G1 DMSO (bright red) N=2, MR 8hrs late G1 ICRF-193 at *t* = 2 hrs/MR 8hrs late G1 DMSO at *t* = 2 hrs (dark red) N=2, MR 8hrs late G1 with ICRF-193 at *t* = 2 hrs with readding at *t*

= 4 hrs and *t* = 6 hrs/MR 8hrs DMSO at *t* = 2 hrs with readding at *t* = 4 hrs and *t* = 6 hrs (beige). N=3. 250kb binned data. Bar graph shows mean of two biological replicates, scatterplot overlay shows values from individual replicates. With and without re-adding samples are from separate experiments.

I. Schematic of HeLa S3 mitotic synchronization and release experiment with ICRF-193 treatment starting at *t* = 2 hrs, *t* = 3 hrs, or *t* = 4 hrs post mitotic release, collected after 5 hours of treatment, with sorting for G1 DNA content. HeLa S3 cells were synchronized in S phase by 24hr treatment with 2mM thymidine, released three hours, then arrested in prometaphase with a 12hr treatment with nocodazole. Mitotic cells were collected by mitotic shake-off, washed, and released into fresh media. DMSO or 30uM ICRF-193 was added *t* = 2 hrs, *t* = 3 hrs, or *t* = 4 hrs after mitotic release. Adherent cells were fixed after five hours total treatment (Late G1, *t* = 7 hrs, *t* = 8 hrs, or *t* = 9 hrs timepoints) for Hi-C 2.0 with 1% FA. Cells with G1 DNA content isolated by FACS. Chromosome structure of G1 sorted cells was analyzed by Hi-C 2.0 with DpnII digestion. 2 biological replicates were performed.

J. Flow cytometry profiles for DNA content (PI stain) of synchronized HeLa S3 cells released into G1 at *t* = 2 hrs, *t* = 3 hrs, or *t* = 4 hrs, or with DMSO or 30uM ICRF-193 from *t* = 2 hrs to *t* = 7 hrs, *t* = 3 hrs to *t* = 8 hrs, or *t* = 4 hrs to *t* = 9 hrs (5 hour total treatment for each). Hi-C was performed on G1 sorted population. Replicate one shown in main figure, replicate two shown in Supp 3.

K. Hi-C interaction heatmaps of G1 sorted MR HeLa S3 cells treated with DMSO or 30uM ICRF-193 from *t* = 2 hrs to *t* = 7 hrs, *t* = 3 hrs to *t* = 8 hrs, or *t* = 4 hrs to *t* = 9 hrs after mitotic release for the q arm of Chr14. Binned at 250kb with iterative correction

and read normalized between samples, two replicates combined. Eigenvector 1 is plotted below each heatmap.

L. Hi-C interaction log10 ratio heatmap comparing ICRF-193 treatment to DMSO control for each treatment type, 250kb bins. Two replicates combined.

M. AA Hi-C compartment strength log2 ratio compared to DMSO by distance, separated by compartment type, for HeLa S3 cells. MR 2-7hrs late G1 ICRF-193/ MR 2-7hrs late G1 DMSO (dark red), MR 3-6hrs late G1 ICRF-193/MR 3-6hrs late G1 DMSO (pink), MR 4-9hrs late G1 ICRF-193/ MR 4-9hrs late G1 DMSO (beige). N=2. 250kb binned data. Bar graph shows mean of two biological replicates, scatterplot overlay shows values from individual replicates.

N. BB Hi-C compartment strength log2 ratio compared to DMSO by distance, separated by compartment type, for HeLa S3 cells. MR 2-7hrs late G1 ICRF-193/ MR 2-7hrs late G1 DMSO (dark red), MR 3-6hrs late G1 ICRF-193/MR 3-6hrs late G1 DMSO (pink), MR 4-9hrs late G1 ICRF-193/ MR 4-9hrs late G1 DMSO (beige). N=2. 250kb binned data. Bar graph shows mean of two biological replicates, scatterplot overlay shows values from individual replicates.

**Figure 4: Topo II resolves mitotic entanglements during G1 establishment of interphase chromosome folding**

A. Schematic of cell synchronization and MC-3C protocol. MC-3C was performed on HeLa S3 cells during prometaphase arrest ($t$ = 0) or after mitotic release at $t$ = 2 hrs (anaphase/telophase), $t$ = 4 hrs (early G1), or $t$ = 8 hrs (late G1). The early and late G1

timepoints had DMSO or 30uM ICRF-193 added at *t* = 2 hrs post mitotic release, and were G1 sorted after fixation.

B. Fraction of C-walks within one chromosome or between two chromosomes, and in A, B, or both A and B compartments, out of the first 6 fragments of all one and two chromosome C-walks. Three biological replicates are shown separately.

C. Density plot of the direct pairwise interaction distances from MC-3C C-walks, for the first 6 fragments of 1 chromosome C-walks assigned to A, B, or both A and B compartments. Three replicates are combined for each sample. Bracket shows the region where ICRF-193 treatment results in retained mitotic interactions compared in early G1 compared to DMSO treatment.

D. Density plot of pairwise interaction distance from sampled Hi-C libraries made from *t* = 0 prometaphase and *t* = 2 hrs anaphase/telophase unsorted cells, and G1 sorted early and late G1 cells with DMSO or 30uM ICRF-193 treatment. The *t* = 0 prometaphase and *t* = 2 hrs Hi-C libraries are the same as shown in Figure S3F-H, while the early and late G1 libraries are the same as shown in Figure 1 (G-J). Only reads on intact chromosomes with an assigned compartment type were used. Two replicates are combined for each sample. Bracket shows the region where ICRF-193 treatment results in retained mitotic interactions compared in early G1 compared to DMSO treatment.

E. Schematic of different types of interfaces between different genomic regions on the same chromosome. A smooth interface (top) will result in a C-walk (black dashed arrow) with most steps within each region, and fewer steps between the two regions (indicated by small black solid arrow). An entangled/intermingled interface (bottom) will result in a

C-walk (black dashed arrow) with more steps between the two regions (indicated by small black solid arrows).

F. Schematic of the two possible types of two region C-walks considered for calculation of the Intermingling Metric (IM). Regions are defined as either side of the largest step (*x*) within each C-walk, with each side extending ¼ of the size of the largest step upstream and downstream of the midpoint of fragment at either end of the largest step (so each region has a maximum size of ½ the largest step size (0.5*x*)).

G. Formula of the IM calculation for determining how much intermingling/entanglement occurs between two regions. The IM is calculated as the fraction of C-walks with >1 inter-region step.

H. Intermingling analysis of control cells during mitotic exit. Central diagonal: Heatmaps of the IM over a range of sliding window sizes (4-16Mb), for regions separated by 0-30Mb for *t* = 0 Prometa, *t* = 2 hrs, *t* = 4 hrs early G1 DMSO, and *t* = 8 hrs late G1 DMSO samples. The mean of three biological replicates is shown. Top triangle: Heatmaps of the log2 fold change of pairwise comparisons of the IM of the samples shown on the diagonal, over a range of sliding window sizes (4-16Mb), for regions separated by 0-30Mb. The mean of three biological replicates is shown. Bottom triangle: Pairwise comparisons of the IM of the samples shown on the diagonal as line plots for the 12Mb window size. Mean (darker line) +/- 95% CI (lighter filled areas) of three biological replicates is shown for the real C-walks. Permuted C-walks (100 permutations per sample x 3 replicates each) are also plotted, with the mean of all 300 permutations for each sample shown as dashed lines, and 95% CI shown by the surrounding filled areas.

Bracket indicates the area of significant difference between *t* = 2 hrs and *t* = 4 hrs early G1 DMSO.

I. Intermingling analysis of ICRF-193 treated cells. Left column: Heatmaps of IM over a range of sliding window sizes (4-16Mb), for regions separated by 0-30Mb for *t* = 4 hrs early G1 ICRF-193 and *t* = 8 hrs late G1 ICRF-193 samples. The mean of three biological replicates is shown. Second column: Heatmaps of the log2 fold change of the IM for ICRF-193 vs DMSO for the early or late G1 timepoints, over a range of sliding window sizes (4-16Mb), for regions separated by 0-30Mb. The mean of three biological replicates is shown. Third column: Comparisons of the IM for ICRF-193 vs DMSO for the early or late G1 timepoints. Line plots for the 12Mb window size. Mean (darker line) +/- 95% CI (lighter filled areas) of three biological replicates is shown for the real C-walks. Permuted C-walks (100 permutations per sample x 3 replicates each) are also plotted, with the mean of all 300 permutations for each sample shown as dashed lines, and 95% CI shown by the surrounding filled areas. Bracket indicates the area of significant difference between *t* = 4 hrs early G1 DMSO and *t* = 4 hrs early G1 ICRF-193. Fourth column: Heatmaps of the log2 fold change of the IM for early or late G1 ICRF-193 vs *t* = 2 hrs anaphase/telophase, over a range of sliding window sizes (4-16Mb), for regions separated by 0-30Mb. The mean of three biological replicates is shown. Fifth column: Comparisons of the IM for early or late G1 ICRF-193 vs *t* = 2 hrs anaphase/telophase. Line plots for the 12Mb window size. Mean (darker line) +/- 95% CI (lighter filled areas) of three biological replicates is shown for the real C-walks. Permuted C-walks (100 permutations per sample x 3 replicates each) are also plotted,

with the mean of all 300 permutations for each sample shown as dashed lines, and 95% CI shown by the surrounding filled areas.

**Figure 5. Polymer simulations reveal that hallmarks of mitotic exit with inhibited Topoisomerase II correspond to the entangled mitotic chromosome**

A. Two topologies of mitotic (initial) state considered in polymer simulations: non-catenated condensin loops (left) and catenated condensin loops (right). Contact maps (averaged over 8 replicates) and the matrices of pairwise linking numbers are shown for each state. The snapshots of the two states are demonstrated: condensin loops (gray) form a dense bottlebrush array; the loop bases comprise the spiraled backbone (red); two loops ($45^{th}$ and $100^{th}$), colored by pink and green correspondingly, are non-catenated in the left state and are catenated in the right state. Catenation of the two loops in the catenated state is denoted by red dots on the matrix of pairwise linking numbers (right). Mean number of catenations of one condensin loop with all other loops and the corresponding standard deviation (in the ensemble of all loops in all replicates) are indicated below the matrix.

B. The simulated contact matrices for catenated (right) and non-catenated (left) initial states for early ($\approx 1$ hour) and late ($\approx 8$ hours) interphase in different resolutions: 80Mb (0-80Mb), 20Mb (8-28Mb) and 8Mb (8-16Mb) segments. Contact maps were averaged over 8 replicates and over time ($\approx 30\mathrm{min}$).

C. The saddle plots for the contact matrices (80Mb) from panel B are demonstrated. The corresponding compartmental scores (AA+BB)/(AB+BA) are indicated. Saddle plots

are binned into 50 bins and the scores are calculated for the corner 10 bins of A and B compartments.

D. The contact probability curve and its log-derivative for the two mitotic states.

E. Evolution of the contact probability curves with the log-derivatives in the mitotic exit: mitosis (gray), early and late G1 curves for different initial states. The colors are shown in the legend above the plot. Expansion from the non-catenated state results in a much weaker band, as reflected by the magnitude of the hump of the log-derivative of P(s) at $\approx 10Mb$.

F. Kinetics of the chromosomal territoriality for the two initial states, measured as cis/trans ratio in simulations. The contacts were registered for two values of the contact radius: 3 and 5 monomers (≈90 nm and ≈150 nm, correspondingly), which correspond to the edges of the error bars (black). The interval of MC-3C cis/trans ratios for various chromosomes for the ICRF-193 experiment (time point t=4h; inhibition of Topo II activity is done at 2h) is indicated.

**Figure 6. The two-stage model of mitotic exit allows for directed Topo II and removal of most of the mitotic catenations**

A. The contact probability P(s) and its log-derivative for the instantaneous one-stage mitotic exit and without extrusion reveals fast entanglement of chromosomal segments to the level of ideal chain, i.e. $P(s) \sim s^{-3/2}$, in several hours.

B. Activity of Topo II can swiftly mix the chromosomes in cis and trans during instantaneous (one-stage) mitotic exit: cylindrical constraints and condensin loops are released at one time under allowed random strand passage. Snapshots of four

chromosomes (PBC images) from simulations in the initial and final states are shown in different colors.

C. Kinetics of territoriality (cis/trans ratios) during the one-stage exit for polymer simulations with and without cohesin extrusion. The contacts were registered for two values of the contact radius: 3 and 5 monomers (≈90 nm and ≈150 nm, correspondingly), which correspond to the edges of the error bars (red). The interval of MC-3C cis/trans ratios for various chromosomes for the DMSO experiment (time point t=4h; addition of DMSO is done at 2h) is indicated.

D. Two-stage exit: bottlebrush swelling can direct activity of Topo II and decatenate most of the mitotic loops in the wild type. During the first stage condensin loops are kept on the chromosome, while cylindrical constraints are released under allowed strand passage. During the second stage condensin loops are released and the strand passage activity is reduced, emulating weakened Topo II activity. The snapshots of initial mitotic, early telophase and final interphase states are shown. Matrices of the pairwise linking numbers of condensin loops for the mitotic and telophase states demonstrate massive decatenation of the loops during the first stage. Cohesin extrusion and compartments are added into the simulation in the second stage, as shown in the legend for the snapshot at the right.

E. Mean number of cis (red) and trans (blue) catenations per loop as a function of duration of the first stage of the two-stage exit; 8 replicates are shown (thin) and their average (bold). The topological steady-state, i.e. when the number of catenations saturates, is achieved in 1-2 hours.

F. Territorialities of simulated chromosomes expanded via the two-stage mechanism as a function of time from the beginning of expansion. Stripes, corresponding to two values of the contact radius (90 nm and 150 nm), are shown for three durations of the first stage as indicated in the legend. The interval of MC-3C cis/trans ratios for various chromosomes for the DMSO experiment (time point t=4h; DMSO is added at 2h) is indicated.

G. The contact probability and its log-derivative after the removal of cohesin loops from the late interphase state (~ 8 hours after the expansion) obtained by the two-stage mechanism. Curves for different durations of the first stage are shown by different colors. Almost full decatenation during the first stage (T=2h) results in a “fractal globule” scaling of P(s) after cohesin knock-out in the late interphase.

H. Snapshots of two chains at 3 hours from mitosis resulting from expansion via the two-stage mechanism (duration of the first stage, T=2h; left) and one-stage mechanism (right). In both cases cohesin is removed from the chain, which corresponds to P(s) scalings in Figure 6G (red) and Figure 6A, respectively. The chain is colored from red to purple along the contour to demonstrate crumpledness of the segments in the first case and its mixing in the second.

I. Simulated contact maps for three states in the process of two-stage exit from the entangled mitosis: mitotic, anaphase/telophase and interphase. The anaphase/telophase contact map and the resulting interphase map correspond to duration of the first stage T=2h. Each contact map is obtained as the result of averaging over 8 replicates and over time (30 min).

**Figure 7: Cohesin directs Topo II activity to disentangle long-range compartment interactions**

A. Schematic of RAD21 degradation and Topo II inhibition by ICRF-193 in AS HCT116 + RAD21-AID-mClover (HCT116 + RAD21-mAC) cells for Hi-C or MC-3C. Cells were treated for 2 hours with IAA and/or ICRF-193 before fixation for Hi-C or MC-3C, and sorting for G1 DNA content with (- IAA samples) or without (+ IAA samples) mClover.

B. Aggregate loop pileup of experiment shown in A. at dots called in published high resolution Hi-C data from HCT116 + RAD21-mAC (Untreated) (4DNFIFLDVASC). Average log2(observed/expected) is shown in the first 4 columns, and log2 fold change of each treatment vs the control is shown in the last 3 columns. 10kb bins. Three replicates combined.

C. Hi-C interaction heatmaps of HCT116 + RAD21-mAC cells described in A, for Chr5:0-40Mb. Binned at 250kb with iterative correction and read normalized between samples, three replicates combined. Eigenvector 1 is plotted below each heatmap.

D. Hi-C interaction log2 ratio heatmap for Chr5:0-40Mb comparing each treatment to the Control or to the IAA treatment, as indicated, 250kb bins. Three replicates combined.

E. P(*s*) scaling plot of G1 sorted HCT116 + RAD21-mAC cells described in A. DMSO (bright blue), IAA (purple), ICRF-193 (bright red), IAA + ICRF-193 (gold). Three replicates combined.

F. First derivative (slope) of P(*s*) scaling plot shown in E. Three replicates combined.

G. AA compartment strength log2 ratio compared to Control by distance for HCT116 + RAD21-mAC cells, IAA/Control (purple), ICRF-193/Control (red), IAA + ICRF-

193/Control (gold). N=3. 250kb binned data. Bar graph shows mean of three biological replicates, scatterplot overlay shows values from individual replicates.

H. BB compartment strength log2 ratio compared to Control by distance for HCT116 + RAD21-mAC cells, IAA/Control (purple), ICRF-193/Control (red), IAA + ICRF-193/Control (gold). N=3. 250kb binned data. Bar graph shows mean of three biological replicates, scatterplot overlay shows values from individual replicates.

I. Density plot of C-walk span for the first 6 fragments of 1 chromosome C-walks assigned to A, B, or both A and B compartments. Samples: DMSO (bright blue), IAA (purple), ICRF-193 (bright red), IAA + ICRF-193 (gold).

J. Density plot of direct pairwise interaction distances from MC-3C reads, for the first 6 fragments of 1 chromosome C-walks assigned to A, B, or both A and B compartments. Samples: DMSO (bright blue), IAA (purple), ICRF-193 (bright red), IAA + ICRF-193 (gold).

K. Intermingling analysis of HCT116 + RAD21-mAC cells with or without Topo II inhibition, as described in A. All compartment types combined. IM as line plots for the 12Mb window size. Mean (darker line) +/- 95% CI (lighter filled areas) of three biological replicates is shown for the real C-walks. Permuted C-walks (100 permutations per sample x 3 replicates each) are also plotted, with the mean of all 300 permutations for each sample shown as dashed lines, and 95% CI shown by the surrounding filled areas. Samples: DMSO (bright blue), IAA (purple), ICRF-193 (bright red), IAA + ICRF-193 (gold).

L. Intermingling analysis of HCT116 + RAD21-mAC cells with or without Topo II inhibition, as described in A. C-walks separated by compartment type into A (top), A and

B (middle) and B (bottom). IM as line plots for the 12Mb window size. Mean (darker line) +/- 95% CI (lighter filled areas) of three biological replicates is shown for the real C-walks. Permuted C-walks (100 permutations per sample x 3 replicates each) are also plotted, with the mean of all 300 permutations for each sample shown as dashed lines, and 95% CI shown by the surrounding filled areas. Samples: IAA (purple), ICRF-193 (bright red).

M. Model: Control of chromosomal entanglements through the cell cycle by interplay between Topoisomerase II, chromosome decondensation, and cohesin mediated loop extrusion. Mitotic chromosomes contain self-catenations between regions that will become separate A and B compartments in G1. These entanglements require Topo II to be removed as chromosomes decondense during G1 entry for correct timing of chromosome compartment establishment. During interphase, loop extrusion by the cohesin complex directs Topo II activity to prevent entanglements from occurring between distal compartment domains of the same type (e.g. A-A or B-B).

## DATA AVAILABILITY

Hi-C and MC-3C sequencing data generated for this study will be available on GEO upon publication. Microscopy data will be available in the BioStudies database[129].

## CODE AVAILABILITY

Examples of custom scripts used for Hi-C and MC-3C will be available on github upon publication. Microscopy image analysis CellProfiler pipelines and python scripts will be

available in the BioStudies database upon publication[129]. Scripts for computational modeling will be available on github upon publication.

## ACKNOWLEDGEMENTS

We are grateful to Masato Kanemaki for kindly providing the HCT-116-Rad21-mAID-mClover cell line. We thank several UMass Chan Medical School Facilities for their assistance, including Christina Baer at the Sanderson Center for Optical Experimentation, the Deep Sequencing Core, the PacBio Core Enterprise, the Molecular Biology Core Labs, and the Flow Cytometry Core. We thank Caryn Navarro, Caroline Austin, and members of J.D.'s and L.M.'s groups for helpful discussions and comments on the manuscript. Diagrams included in figures were created with BioRender.com. Experiments in this study used a HeLa cell line. Henrietta Lacks, and the HeLa cell line that was established from her tumor cells without her knowledge or consent in 1951, have made significant contributions to scientific progress and advances in human health. We are grateful to Henrietta Lacks, now deceased, and to her surviving family members for their contributions to biomedical research. We also thank the anonymous patient who contributed the HCT 116 cell line used in this study. We acknowledge support from the National Institutes of Health Common Fund 4D Nucleome Program (DK107980, HG011536) and the National Human Genome Research Institute (HG003143). J.D. is an investigator of the Howard Hughes Medical Institute. E.H. was supported by an F32 fellowship from the NIH (F32-CA224689). The work of K.P. is supported by the Russian Science Foundation (Grant No. 21-73-00176).

K.P. acknowledges hospitality of LPTMS laboratory (University of Paris-Saclay), where part of this work was written.

## PUBLISHED DATASETS USED

4DNFIFLDVASC, 4DNFIBM9QCFG

## AUTHOR CONTRIBUTIONS

EH, JD, KP, and LM conceived of the project. EH performed most experiments and analysis. KP performed the computational modeling. EH and YLiu performed Hi-C experiments. EH performed MC-3C experiments. EH analyzed Hi-C data. EH analyzed MC-3C data, with contributions from BD, SV, and KP. EH, DL, and YLing performed wide-field microscopy experiments and analysis. EH performed confocal microscopy experiments and analysis. NF constructed the HeLa + Top2A-Venus cell line. JD supervised the experiments and analysis, LM supervised the computational modeling. EH compiled the data and wrote the manuscript with input from all coauthors.

## COMPETING INTERESTS

No competing interests are declared.

## REFERENCES

1. Pommier, Y., Sun, Y., Huang, S.N., and Nitiss, J.L. (2016). Roles of eukaryotic topoisomerases in transcription, replication and genomic stability. Nat Rev Mol Cell Biol *17*, 703-721. 10.1038/nrm.2016.111.
2. Austin, C.A., and Fisher, L.M. (1990). Isolation and characterization of a human cDNA clone encoding a novel DNA topoisomerase II homologue from HeLa cells. FEBS Lett *266*, 115-117. 10.1016/0014-5793(90)81520-x.

3. Lewis, C.D., and Laemmli, U.K. (1982). Higher order metaphase chromosome structure: evidence for metalloprotein interactions. Cell *29*, 171-181. 10.1016/0092-8674(82)90101-5.
4. Earnshaw, W.C., and Heck, M.M. (1985). Localization of topoisomerase II in mitotic chromosomes. J Cell Biol *100*, 1716-1725. 10.1083/jcb.100.5.1716.
5. Earnshaw, W.C., Halligan, B., Cooke, C.A., Heck, M.M., and Liu, L.F. (1985). Topoisomerase II is a structural component of mitotic chromosome scaffolds. J Cell Biol *100*, 1706-1715. 10.1083/jcb.100.5.1706.
6. Drake, F.H., Zimmerman, J.P., McCabe, F.L., Bartus, H.F., Per, S.R., Sullivan, D.M., Ross, W.E., Mattern, M.R., Johnson, R.K., Crooke, S.T., and et al. (1987). Purification of topoisomerase II from amsacrine-resistant P388 leukemia cells. Evidence for two forms of the enzyme. J Biol Chem *262*, 16739-16747.
7. Wang, J.C. (2002). Cellular roles of DNA topoisomerases: a molecular perspective. Nat Rev Mol Cell Biol *3*, 430-440. 10.1038/nrm831.
8. Austin, C.A., Barot, H., Margerrison, E.E.C., Hayes, M.V., and Fisher, L.M. (1989). Biochemical and immunological characterization of mammalian DNA topoisomerase II. Biochemical Society Transactions *17*, 528-529. 10.1042/bst0170528.
9. Tsai-Pflugfelder, M., Liu, L.F., Liu, A.A., Tewey, K.M., Whang-Peng, J., Knutsen, T., Huebner, K., Croce, C.M., and Wang, J.C. (1988). Cloning and sequencing of cDNA encoding human DNA topoisomerase II and localization of the gene to chromosome region 17q21-22. Proc Natl Acad Sci U S A *85*, 7177-7181. 10.1073/pnas.85.19.7177.
10. Broderick, R., and Niedzwiedz, W. (2015). Sister chromatid decatenation: bridging the gaps in our knowledge. Cell Cycle *14*, 3040-3044. 10.1080/15384101.2015.1078039.
11. Bower, J.J., Karaca, G.F., Zhou, Y., Simpson, D.A., Cordeiro-Stone, M., and Kaufmann, W.K. (2010). Topoisomerase IIalpha maintains genomic stability through decatenation G(2) checkpoint signaling. Oncogene *29*, 4787-4799. 10.1038/onc.2010.232.
12. Luo, K., Yuan, J., Chen, J., and Lou, Z. (2009). Topoisomerase IIalpha controls the decatenation checkpoint. Nat Cell Biol *11*, 204-210. 10.1038/ncb1828.
13. Samejima, K., Samejima, I., Vagnarelli, P., Ogawa, H., Vargiu, G., Kelly, D.A., de Lima Alves, F., Kerr, A., Green, L.C., Hudson, D.F., et al. (2012). Mitotic chromosomes are compacted laterally by KIF4 and condensin and axially by topoisomerase IIalpha. J Cell Biol *199*, 755-770. 10.1083/jcb.201202155.
14. Warburton, P.E., and Earnshaw, W.C. (1997). Untangling the role of DNA topoisomerase II in mitotic chromosome structure and function. Bioessays *19*, 97-99. 10.1002/bies.950190203.
15. Moens, P.B., and Earnshaw, W.C. (1989). Anti-topoisomerase II recognizes meiotic chromosome cores. Chromosoma *98*, 317-322. 10.1007/BF00292383.
16. Heck, M.M., and Earnshaw, W.C. (1986). Topoisomerase II: A specific marker for cell proliferation. J Cell Biol *103*, 2569-2581. 10.1083/jcb.103.6.2569.
17. Heck, M.M., Hittelman, W.N., and Earnshaw, W.C. (1988). Differential expression of DNA topoisomerases I and II during the eukaryotic cell cycle. Proc Natl Acad Sci U S A *85*, 1086-1090. 10.1073/pnas.85.4.1086.

18. Gasser, S.M., Laroche, T., Falquet, J., Boy de la Tour, E., and Laemmli, U.K. (1986). Metaphase chromosome structure. Involvement of topoisomerase II. J Mol Biol *188*, 613-629. 10.1016/s0022-2836(86)80010-9.
19. Gasser, S.M., and Laemmli, U.K. (1986). The organisation of chromatin loops: characterization of a scaffold attachment site. EMBO J *5*, 511-518. 10.1002/j.1460-2075.1986.tb04240.x.
20. Mirkovitch, J., Gasser, S.M., and Laemmli, U.K. (1988). Scaffold attachment of DNA loops in metaphase chromosomes. J Mol Biol *200*, 101-109. 10.1016/0022-2836(88)90336-1.
21. Canela, A., Maman, Y., Huang, S.N., Wutz, G., Tang, W., Zagnoli-Vieira, G., Callen, E., Wong, N., Day, A., Peters, J.M., et al. (2019). Topoisomerase II-Induced Chromosome Breakage and Translocation Is Determined by Chromosome Architecture and Transcriptional Activity. Mol Cell *75*, 252-266 e258. 10.1016/j.molcel.2019.04.030.
22. Canela, A., Maman, Y., Jung, S., Wong, N., Callen, E., Day, A., Kieffer-Kwon, K.R., Pekowska, A., Zhang, H., Rao, S.S.P., et al. (2017). Genome Organization Drives Chromosome Fragility. Cell *170*, 507-521 e518. 10.1016/j.cell.2017.06.034.
23. Canela, A., Sridharan, S., Sciascia, N., Tubbs, A., Meltzer, P., Sleckman, B.P., and Nussenzweig, A. (2016). DNA Breaks and End Resection Measured Genome-wide by End Sequencing. Mol Cell *63*, 898-911. 10.1016/j.molcel.2016.06.034.
24. Uuskula-Reimand, L., Hou, H., Samavarchi-Tehrani, P., Rudan, M.V., Liang, M., Medina-Rivera, A., Mohammed, H., Schmidt, D., Schwalie, P., Young, E.J., et al. (2016). Topoisomerase II beta interacts with cohesin and CTCF at topological domain borders. Genome Biol *17*, 182. 10.1186/s13059-016-1043-8.
25. Manville, C.M., Smith, K., Sondka, Z., Rance, H., Cockell, S., Cowell, I.G., Lee, K.C., Morris, N.J., Padget, K., Jackson, G.H., and Austin, C.A. (2015). Genome-wide ChIP-seq analysis of human TOP2B occupancy in MCF7 breast cancer epithelial cells. Biol Open *4*, 1436-1447. 10.1242/bio.014308.
26. Lieberman-Aiden, E., van Berkum, N.L., Williams, L., Imakaev, M., Ragoczy, T., Telling, A., Amit, I., Lajoie, B.R., Sabo, P.J., Dorschner, M.O., et al. (2009). Comprehensive mapping of long-range interactions reveals folding principles of the human genome. Science *326*, 289-293. 10.1126/science.1181369.
27. Tavares-Cadete, F., Norouzi, D., Dekker, B., Liu, Y., and Dekker, J. (2020). Multi-contact 3C reveals that the human genome during interphase is largely not entangled. Nat Struct Mol Biol *27*, 1105-1114. 10.1038/s41594-020-0506-5.
28. Goundaroulis, D., Lieberman Aiden, E., and Stasiak, A. (2020). Chromatin Is Frequently Unknotted at the Megabase Scale. Biophys J *118*, 2268-2279. 10.1016/j.bpj.2019.11.002.
29. Kawamura, R., Pope, L.H., Christensen, M.O., Sun, M., Terekhova, K., Boege, F., Mielke, C., Andersen, A.H., and Marko, J.F. (2010). Mitotic chromosomes are constrained by topoisomerase II-sensitive DNA entanglements. J Cell Biol *188*, 653-663. 10.1083/jcb.200910085.

30. Rosa, A., Di Stefano, M., and Micheletti, C. (2019). Topological Constraints in Eukaryotic Genomes and How They Can Be Exploited to Improve Spatial Models of Chromosomes. Front Mol Biosci *6*, 127. 10.3389/fmolb.2019.00127.
31. Rosa, A., and Everaers, R. (2008). Structure and dynamics of interphase chromosomes. PLoS Comput Biol *4*, e1000153. 10.1371/journal.pcbi.1000153.
32. Sikorav, J.L., and Jannink, G. (1994). Kinetics of chromosome condensation in the presence of topoisomerases: a phantom chain model. Biophys J *66*, 827-837. 10.1016/s0006-3495(94)80859-8.
33. Nielsen, C.F., Zhang, T., Barisic, M., Kalitsis, P., and Hudson, D.F. (2020). Topoisomerase IIalpha is essential for maintenance of mitotic chromosome structure. Proc Natl Acad Sci U S A *117*, 12131-12142. 10.1073/pnas.2001760117.
34. Morris, S.K., Baird, C.L., and Lindsley, J.E. (2000). Steady-state and rapid kinetic analysis of topoisomerase II trapped as the closed-clamp intermediate by ICRF-193. J Biol Chem *275*, 2613-2618. 10.1074/jbc.275.4.2613.
35. Roca, J., Ishida, R., Berger, J.M., Andoh, T., and Wang, J.C. (1994). Antitumor bisdioxopiperazines inhibit yeast DNA topoisomerase II by trapping the enzyme in the form of a closed protein clamp. Proc Natl Acad Sci U S A *91*, 1781-1785. 10.1073/pnas.91.5.1781.
36. Shapiro, A.B., and Austin, C.A. (2014). A high-throughput fluorescence anisotropy-based assay for human topoisomerase II beta-catalyzed ATP-dependent supercoiled DNA relaxation. Anal Biochem *448*, 23-29. 10.1016/j.ab.2013.11.029.
37. Ishida, R., Sato, M., Narita, T., Utsumi, K.R., Nishimoto, T., Morita, T., Nagata, H., and Andoh, T. (1994). Inhibition of DNA topoisomerase II by ICRF-193 induces polyploidization by uncoupling chromosome dynamics from other cell cycle events. J Cell Biol *126*, 1341-1351. 10.1083/jcb.126.6.1341.
38. Iwai, M., Hara, A., Andoh, T., and Ishida, R. (1997). ICRF-193, a catalytic inhibitor of DNA topoisomerase II, delays the cell cycle progression from metaphase, but not from anaphase to the G1 phase in mammalian cells. FEBS Lett *406*, 267-270. 10.1016/s0014-5793(97)00282-2.
39. Clarke, D.J., Johnson, R.T., and Downes, C.S. (1993). Topoisomerase II inhibition prevents anaphase chromatid segregation in mammalian cells independently of the generation of DNA strand breaks. J Cell Sci *105 ( Pt 2)*, 563-569.
40. Gimenez-Abian, J.F., and Clarke, D.J. (2009). Cytological analysis of chromosome structural defects that result from topoisomerase II dysfunction. Methods Mol Biol *582*, 189-207. 10.1007/978-1-60761-340-4_15.
41. Gimenez-Abian, J.F., Lane, A.B., and Clarke, D.J. (2018). Analyzing Mitotic Chromosome Structural Defects After Topoisomerase II Inhibition or Mutation. Methods Mol Biol *1703*, 191-215. 10.1007/978-1-4939-7459-7_15.
42. Gimenez-Abian, J.F., Clarke, D.J., Gimenez-Martin, G., Weingartner, M., Gimenez-Abian, M.I., Carballo, J.A., Diaz de la Espina, S.M., Bogre, L., and De la Torre, C. (2002). DNA catenations that link sister chromatids until the onset of anaphase are maintained by a checkpoint mechanism. Eur J Cell Biol *81*, 9-16. 10.1078/0171-9335-00226.

43. Zhang, S., Ubelmesser, N., Josipovic, N., Forte, G., Slotman, J.A., Chiang, M., Gothe, H.J., Gusmao, E.G., Becker, C., Altmuller, J., et al. (2021). RNA polymerase II is required for spatial chromatin reorganization following exit from mitosis. Sci Adv *7*, eabg8205. 10.1126/sciadv.abg8205.
44. Belaghzal, H., Dekker, J., and Gibcus, J.H. (2017). Hi-C 2.0: An optimized Hi-C procedure for high-resolution genome-wide mapping of chromosome conformation. Methods *123*, 56-65. 10.1016/j.ymeth.2017.04.004.
45. Tanabe, K., Ikegami, Y., Ishida, R., and Andoh, T. (1991). Inhibition of topoisomerase II by antitumor agents bis(2,6-dioxopiperazine) derivatives. Cancer Res *51*, 4903-4908.
46. Naughton, C., Avlonitis, N., Corless, S., Prendergast, J.G., Mati, I.K., Eijk, P.P., Cockroft, S.L., Bradley, M., Ylstra, B., and Gilbert, N. (2013). Transcription forms and remodels supercoiling domains unfolding large-scale chromatin structures. Nat Struct Mol Biol *20*, 387-395. 10.1038/nsmb.2509.
47. Abramo, K., Valton, A.L., Venev, S.V., Ozadam, H., Fox, A.N., and Dekker, J. (2019). A chromosome folding intermediate at the condensin-to-cohesin transition during telophase. Nat Cell Biol *21*, 1393-1402. 10.1038/s41556-019-0406-2.
48. Naumova, N., Imakaev, M., Fudenberg, G., Zhan, Y., Lajoie, B.R., Mirny, L.A., and Dekker, J. (2013). Organization of the mitotic chromosome. Science *342*, 948-953. 10.1126/science.1236083.
49. Zhang, H., Emerson, D.J., Gilgenast, T.G., Titus, K.R., Lan, Y., Huang, P., Zhang, D., Wang, H., Keller, C.A., Giardine, B., et al. (2019). Chromatin structure dynamics during the mitosis-to-G1 phase transition. Nature *576*, 158-162. 10.1038/s41586-019-1778-y.
50. Gibcus, J.H., Samejima, K., Goloborodko, A., Samejima, I., Naumova, N., Nuebler, J., Kanemaki, M.T., Xie, L., Paulson, J.R., Earnshaw, W.C., et al. (2018). A pathway for mitotic chromosome formation. Science *359*. 10.1126/science.aao6135.
51. Rao, S.S., Huntley, M.H., Durand, N.C., Stamenova, E.K., Bochkov, I.D., Robinson, J.T., Sanborn, A.L., Machol, I., Omer, A.D., Lander, E.S., and Aiden, E.L. (2014). A 3D map of the human genome at kilobase resolution reveals principles of chromatin looping. Cell *159*, 1665-1680. 10.1016/j.cell.2014.11.021.
52. Hildebrand, E.M., and Dekker, J. (2020). Mechanisms and Functions of Chromosome Compartmentalization. Trends Biochem Sci *45*, 385-396. 10.1016/j.tibs.2020.01.002.
53. Solovei, I., Kreysing, M., Lanctot, C., Kosem, S., Peichl, L., Cremer, T., Guck, J., and Joffe, B. (2009). Nuclear architecture of rod photoreceptor cells adapts to vision in mammalian evolution. Cell *137*, 356-368. 10.1016/j.cell.2009.01.052.
54. Poleshko, A., Smith, C.L., Nguyen, S.C., Sivaramakrishnan, P., Wong, K.G., Murray, J.I., Lakadamyali, M., Joyce, E.F., Jain, R., and Epstein, J.A. (2019). H3K9me2 orchestrates inheritance of spatial positioning of peripheral heterochromatin through mitosis. Elife *8*. 10.7554/eLife.49278.
55. Falk, M., Feodorova, Y., Naumova, N., Imakaev, M., Lajoie, B.R., Leonhardt, H., Joffe, B., Dekker, J., Fudenberg, G., Solovei, I., and Mirny, L.A. (2019).

Heterochromatin drives compartmentalization of inverted and conventional nuclei. Nature *570*, 395-399. 10.1038/s41586-019-1275-3.
56. Smith, C.L., Lan, Y., Jain, R., Epstein, J.A., and Poleshko, A. (2021). Global chromatin relabeling accompanies spatial inversion of chromatin in rod photoreceptors. Sci Adv *7*, eabj3035. 10.1126/sciadv.abj3035.
57. Xu, J., Ma, H., Jin, J., Uttam, S., Fu, R., Huang, Y., and Liu, Y. (2018). Super-Resolution Imaging of Higher-Order Chromatin Structures at Different Epigenomic States in Single Mammalian Cells. Cell Rep *24*, 873-882. 10.1016/j.celrep.2018.06.085.
58. Champoux, J.J., and Dulbecco, R. (1972). An activity from mammalian cells that untwists superhelical DNA--a possible swivel for DNA replication (polyoma-ethidium bromide-mouse-embryo cells-dye binding assay). Proc Natl Acad Sci U S A *69*, 143-146. 10.1073/pnas.69.1.143.
59. Kouzine, F., Gupta, A., Baranello, L., Wojtowicz, D., Ben-Aissa, K., Liu, J., Przytycka, T.M., and Levens, D. (2013). Transcription-dependent dynamic supercoiling is a short-range genomic force. Nat Struct Mol Biol *20*, 396-403. 10.1038/nsmb.2517.
60. Hsiang, Y.H., Hertzberg, R., Hecht, S., and Liu, L.F. (1985). Camptothecin induces protein-linked DNA breaks via mammalian DNA topoisomerase I. J Biol Chem *260*, 14873-14878.
61. Zhang, H., Lam, J., Zhang, D., Lan, Y., Vermunt, M.W., Keller, C.A., Giardine, B., Hardison, R.C., and Blobel, G.A. (2021). CTCF and transcription influence chromatin structure re-configuration after mitosis. Nat Commun *12*, 5157. 10.1038/s41467-021-25418-5.
62. Bensaude, O. (2011). Inhibiting eukaryotic transcription: Which compound to choose? How to evaluate its activity? Transcription *2*, 103-108. 10.4161/trns.2.3.16172.
63. Abramo, K.N. (2020). Building the Interphase Nucleus: A study on the kinetics of 3D chromosome formation, temporal relation to active transcription, and the role of nuclear RNAs. PhD (University of Massachusetts Chan Medical School).
64. Haralick, R.M., Shanmugam, K., and Dinstein, I.H. (1973). Textural Features for Image Classification. IEEE Transactions on Systems, Man, and Cybernetics *SMC-3*, 610-621. 10.1109/tsmc.1973.4309314.
65. Olivares-Chauvet, P., Mukamel, Z., Lifshitz, A., Schwartzman, O., Elkayam, N.O., Lubling, Y., Deikus, G., Sebra, R.P., and Tanay, A. (2016). Capturing pairwise and multi-way chromosomal conformations using chromosomal walks. Nature *540*, 296-300. 10.1038/nature20158.
66. Rao, S.S.P., Huang, S.C., Glenn St Hilaire, B., Engreitz, J.M., Perez, E.M., Kieffer-Kwon, K.R., Sanborn, A.L., Johnstone, S.E., Bascom, G.D., Bochkov, I.D., et al. (2017). Cohesin Loss Eliminates All Loop Domains. Cell *171*, 305-320 e324. 10.1016/j.cell.2017.09.026.
67. Hsieh, T.-H.S., Cattoglio, C., Slobodyanyuk, E., Hansen, A.S., Darzacq, X., and Tjian, R. (2021). Enhancer-promoter interactions and transcription are maintained upon acute loss of CTCF, cohesin, WAPL, and YY1. bioRxiv *2021.07.14.452365*. doi: https://doi.org/10.1101/2021.07.14.452365.

68. Grosberg, A.Y., Nechaev, S.K., and Shakhnovich, E.I. (1988). The role of topological constraints in the kinetics of collapse of macromolecules. Journal de Physique *49* (*12*). 10.1051/jphys:0198800490120209500.
69. Halverson, J.D., Lee, W.B., Grest, G.S., Grosberg, A.Y., and Kremer, K. (2011). Molecular dynamics simulation study of nonconcatenated ring polymers in a melt. II. Dynamics. J Chem Phys *134*, 204905. 10.1063/1.3587138.
70. Polovnikov, K., Nechaev, S., and Tamm, M.V. (2018). Effective Hamiltonian of topologically stabilized polymer states. Soft Matter *14*, 6561-6570. 10.1039/c8sm00785c.
71. Polovnikov, K.E., Nechaev, S., and Tamm, M.V. (2019). Many-body contacts in fractal polymer chains and fractional Brownian trajectories. Phys Rev E *99*, 032501. 10.1103/PhysRevE.99.032501.
72. Mora-Bermudez, F., Gerlich, D., and Ellenberg, J. (2007). Maximal chromosome compaction occurs by axial shortening in anaphase and depends on Aurora kinase. Nat Cell Biol *9*, 822-831. 10.1038/ncb1606.
73. Grosberg, A.Y., and Khokhlov, A.R. (1994). Stastical Physics of Macromolecules (AIP Press).
74. Halverson, J.D., Lee, W.B., Grest, G.S., Grosberg, A.Y., and Kremer, K. (2011). Molecular dynamics simulation study of nonconcatenated ring polymers in a melt. I. Statics. J Chem Phys *134*, 204904. 10.1063/1.3587137.
75. Halverson, J.D., Smrek, J., Kremer, K., and Grosberg, A.Y. (2014). From a melt of rings to chromosome territories: the role of topological constraints in genome folding. Rep Prog Phys *77*, 022601. 10.1088/0034-4885/77/2/022601.
76. Rosa, A., Becker, N.B., and Everaers, R. (2010). Looping probabilities in model interphase chromosomes. Biophys J *98*, 2410-2419. 10.1016/j.bpj.2010.01.054.
77. Polovnikov, K.E., Belan, S., Imakaev, M., Brandao, H., and Mirny, L. (2022). Fractal polymer with loops recapitulates key features of chromosome organization. bioRxiv, 2022.2002.2001.478588. 10.1101/2022.02.01.478588.
78. Salmena, L., Lam, V., McPherson, J.P., and Goldenberg, G.J. (2001). Role of proteasomal degradation in the cell cycle-dependent regulation of DNA topoisomerase IIalpha expression. Biochem Pharmacol *61*, 795-802. 10.1016/s0006-2952(01)00580-9.
79. Lee, J.H., and Berger, J.M. (2019). Cell Cycle-Dependent Control and Roles of DNA Topoisomerase II. Genes (Basel) *10*. 10.3390/genes10110859.
80. Agostinho, M., Rino, J., Braga, J., Ferreira, F., Steffensen, S., and Ferreira, J. (2004). Human topoisomerase IIalpha: targeting to subchromosomal sites of activity during interphase and mitosis. Mol Biol Cell *15*, 2388-2400. 10.1091/mbc.e03-08-0558.
81. Austin, C.A., Lee, K.C., Swan, R.L., Khazeem, M.M., Manville, C.M., Cridland, P., Treumann, A., Porter, A., Morris, N.J., and Cowell, I.G. (2018). TOP2B: The First Thirty Years. Int J Mol Sci *19*. 10.3390/ijms19092765.
82. Meyer, K.N., Kjeldsen, E., Straub, T., Knudsen, B.R., Hickson, I.D., Kikuchi, A., Kreipe, H., and Boege, F. (1997). Cell cycle-coupled relocation of types I and II topoisomerases and modulation of catalytic enzyme activities. J Cell Biol *136*, 775-788. 10.1083/jcb.136.4.775.

83. Orlandini, E., Marenduzzo, D., and Michieletto, D. (2019). Synergy of topoisomerase and structural-maintenance-of-chromosomes proteins creates a universal pathway to simplify genome topology. Proc Natl Acad Sci U S A *116*, 8149-8154. 10.1073/pnas.1815394116.
84. Dyson, S., Segura, J., Martinez-Garcia, B., Valdes, A., and Roca, J. (2021). Condensin minimizes topoisomerase II-mediated entanglements of DNA in vivo. EMBO J *40*, e105393. 10.15252/embj.2020105393.
85. Roca, J., Dyson, S., Segura, J., Valdes, A., and Martinez-Garcia, B. (2022). Keeping intracellular DNA untangled: A new role for condensin? Bioessays *44*, e2100187. 10.1002/bies.202100187.
86. Nishimura, K., Fukagawa, T., Takisawa, H., Kakimoto, T., and Kanemaki, M. (2009). An auxin-based degron system for the rapid depletion of proteins in nonplant cells. Nat Methods *6*, 917-922. 10.1038/nmeth.1401.
87. Natsume, T., Kiyomitsu, T., Saga, Y., and Kanemaki, M.T. (2016). Rapid Protein Depletion in Human Cells by Auxin-Inducible Degron Tagging with Short Homology Donors. Cell Rep *15*, 210-218. 10.1016/j.celrep.2016.03.001.
88. Liu, Y., and Dekker, J. (2021). Biochemically distinct cohesin complexes mediate positioned loops between CTCF sites and dynamic loops within chromatin domains. bioRxiv *2021.08.24.457555*. doi: https://doi.org/10.1101/2021.08.24.457555.
89. Haarhuis, J.H.I., van der Weide, R.H., Blomen, V.A., Yanez-Cuna, J.O., Amendola, M., van Ruiten, M.S., Krijger, P.H.L., Teunissen, H., Medema, R.H., van Steensel, B., et al. (2017). The Cohesin Release Factor WAPL Restricts Chromatin Loop Extension. Cell *169*, 693-707 e614. 10.1016/j.cell.2017.04.013.
90. Schwarzer, W., Abdennur, N., Goloborodko, A., Pekowska, A., Fudenberg, G., Loe-Mie, Y., Fonseca, N.A., Huber, W., Haering, C.H., Mirny, L., and Spitz, F. (2017). Two independent modes of chromatin organization revealed by cohesin removal. Nature *551*, 51-56. 10.1038/nature24281.
91. Hirano, T., and Mitchison, T.J. (1993). Topoisomerase II does not play a scaffolding role in the organization of mitotic chromosomes assembled in Xenopus egg extracts. J Cell Biol *120*, 601-612. 10.1083/jcb.120.3.601.
92. Adachi, Y., Luke, M., and Laemmli, U.K. (1991). Chromosome assembly in vitro: topoisomerase II is required for condensation. Cell *64*, 137-148. 10.1016/0092-8674(91)90215-k.
93. Farr, C.J., Antoniou-Kourounioti, M., Mimmack, M.L., Volkov, A., and Porter, A.C. (2014). The alpha isoform of topoisomerase II is required for hypercompaction of mitotic chromosomes in human cells. Nucleic Acids Res *42*, 4414-4426. 10.1093/nar/gku076.
94. Shintomi, K., and Hirano, T. (2021). Guiding functions of the C-terminal domain of topoisomerase IIalpha advance mitotic chromosome assembly. Nat Commun *12*, 2917. 10.1038/s41467-021-23205-w.
95. Goloborodko, A., Marko, J.F., and Mirny, L.A. (2016). Chromosome Compaction by Active Loop Extrusion. Biophys J *110*, 2162-2168. 10.1016/j.bpj.2016.02.041.
96. Goloborodko, A., Imakaev, M.V., Marko, J.F., and Mirny, L. (2016). Compaction and segregation of sister chromatids via active loop extrusion. Elife *5*. 10.7554/eLife.14864.

97. Piskadlo, E., and Oliveira, R.A. (2017). A Topology-Centric View on Mitotic Chromosome Architecture. Int J Mol Sci *18*. 10.3390/ijms18122751.
98. Racko, D., Benedetti, F., Goundaroulis, D., and Stasiak, A. (2018). Chromatin Loop Extrusion and Chromatin Unknotting. Polymers (Basel) *10*. 10.3390/polym10101126.
99. Fudenberg, G., Imakaev, M., Lu, C., Goloborodko, A., Abdennur, N., and Mirny, L.A. (2016). Formation of Chromosomal Domains by Loop Extrusion. Cell Rep *15*, 2038-2049. 10.1016/j.celrep.2016.04.085.
100. Schalbetter, S.A., Goloborodko, A., Fudenberg, G., Belton, J.M., Miles, C., Yu, M., Dekker, J., Mirny, L., and Baxter, J. (2017). SMC complexes differentially compact mitotic chromosomes according to genomic context. Nat Cell Biol *19*, 1071-1080. 10.1038/ncb3594.
101. Hafner, A., Park, M., Berger, S.E., Nora, E.P., and Boettiger, A.N. (2022). Beyond TADs: microscopy reveals 2 axes of chromosome organization by CTCF and cohesin. bioRxiv *bioRxiv 2022.07.13.499982*. doi: https://doi.org/10.1101/2022.07.13.499982.
102. Gassler, J., Brandao, H.B., Imakaev, M., Flyamer, I.M., Ladstatter, S., Bickmore, W.A., Peters, J.M., Mirny, L.A., and Tachibana, K. (2017). A mechanism of cohesin-dependent loop extrusion organizes zygotic genome architecture. EMBO J *36*, 3600-3618. 10.15252/embj.201798083.
103. Ou, H.D., Phan, S., Deerinck, T.J., Thor, A., Ellisman, M.H., and O'Shea, C.C. (2017). ChromEMT: Visualizing 3D chromatin structure and compaction in interphase and mitotic cells. Science *357*. 10.1126/science.aag0025.
104. Martinez-Garcia, B., Fernandez, X., Diaz-Ingelmo, O., Rodriguez-Campos, A., Manichanh, C., and Roca, J. (2014). Topoisomerase II minimizes DNA entanglements by proofreading DNA topology after DNA strand passage. Nucleic Acids Res *42*, 1821-1830. 10.1093/nar/gkt1037.
105. Seol, Y., and Neuman, K.C. (2016). The Dynamic Interplay Between DNA Topoisomerases and DNA Topology. Biophys Rev *8*, 221-231. 10.1007/s12551-016-0206-x.
106. Rybenkov, V.V., Ullsperger, C., Vologodskii, A.V., and Cozzarelli, N.R. (1997). Simplification of DNA topology below equilibrium values by type II topoisomerases. Science *277*, 690-693. 10.1126/science.277.5326.690.
107. Ran, F.A., Hsu, P.D., Wright, J., Agarwala, V., Scott, D.A., and Zhang, F. (2013). Genome engineering using the CRISPR-Cas9 system. Nat Protoc *8*, 2281-2308. 10.1038/nprot.2013.143.
108. Goloborodko, A., Venev, S., Abdennur, N., azkalot1, and Tommaso, P.D. (2019). mirnylab/distiller-nf: v0.3.3 (v0.3.3). Zenodo. https://doi.org/10.5281/zenodo.3350937.
109. Venev, S., Abdennur, N., Goloborodko, A., Flyamer, I., Fudenberg, G., Nuebler, J., Galitsyna, A., Akgol, B., Abraham, S., Kerpedjiev, P., and Imakaev, M. (2022). open2c/cooltools: v0.5.1. Zenodo. 10.5281/zenodo.6324229.
110. Ewels, P., Magnusson, M., Lundin, S., and Kaller, M. (2016). MultiQC: summarize analysis results for multiple tools and samples in a single report. Bioinformatics *32*, 3047-3048. 10.1093/bioinformatics/btw354.

111. Abdennur, N., Goloborodko, A., Imakaev, M., Kerpedjiev, P., Fudenberg, G., Oullette, S., Lee, S., Strobelt, H., Gehlenborg, N., and Mirny, L. (2021). open2c/cooler: v0.8.11 (v0.8.11). Zenodo. https://doi.org/10.5281/zenodo.4655850.
112. Abdennur, N., and Mirny, L.A. (2020). Cooler: scalable storage for Hi-C data and other genomically labeled arrays. Bioinformatics *36*, 311-316. 10.1093/bioinformatics/btz540.
113. Goloborodko, A., Abdennur, N., Venev, S., hbbrandao, and gfudenberg (2019). mirnylab/pairtools v0.3.0 (v0.3.0). Zenodo. https://doi.org/10.5281/zenodo.2649383.
114. Abdennur, N., Goloborodko, A., gfudenberg, Imakaev, M., agalitsyna, Venev, S., Abraham, S., Flyamer, I., Spracklin, G., Chumpitaz, L., and Aafke (2022). open2c/bioframe: v0.3.3. Zenodo. 10.5281/zenodo.6317259.
115. Open2C, Abdennur, N., Fudenberg, G., Flyamer, I., Galitsyna, A.A., Goloborodko, A., Imakaev, M., and Venev, S.V. (2022). Bioframe: Operations on Genomic Intervals in Pandas Dataframes. bioRxiv *2022.02.16.480748*. https://doi.org/10.1101/2022.02.16.480748.
116. Reback, J., jbrockmendel, McKinney, W., Bossche, J.V.d., Augspurger, T., Roeschke, M., Hawkins, S., Cloud, P., gfyoung, Sinhrks, et al. (2022). pandas-dev/pandas: Pandas 1.4.2 (v1.4.2). Zenodo. https://doi.org/10.5281/zenodo.6408044.
117. Harris, C.R., Millman, K.J., van der Walt, S.J., Gommers, R., Virtanen, P., Cournapeau, D., Wieser, E., Taylor, J., Berg, S., Smith, N.J., et al. (2020). Array programming with NumPy. Nature *585*, 357-362. 10.1038/s41586-020-2649-2.
118. McKinney, W. (2010). Data Structures for Statistical Computing in Python. pp. 56-61.
119. Virtanen, P., Gommers, R., Oliphant, T.E., Haberland, M., Reddy, T., Cournapeau, D., Burovski, E., Peterson, P., Weckesser, W., Bright, J., et al. (2020). SciPy 1.0: fundamental algorithms for scientific computing in Python. Nat Methods *17*, 261-272. 10.1038/s41592-019-0686-2.
120. Hunter, J.D. (2007). Matplotlib: A 2D Graphics Environment. Computing in Science & Engineering *9*, 90-95. 10.1109/mcse.2007.55.
121. van der Walt, S., Schönberger, J., Nunez-Iglesias, J., Boulogne, F., Warner, J., Yager, N., Gouillart, E., Yu, T., and contributors., t.s.-i. (2014). scikit-image: image processing in Python. PeerJ *2*. https://doi.org/10.7717/peerj.453.
122. team, T.s.d. (2021). mwaskom/seaborn: v0.11.2 (August 2021) (v0.11.2). Zenodo. https://doi.org/10.5281/zenodo.5205191.
123. Imakaev, M., Fudenberg, G., McCord, R.P., Naumova, N., Goloborodko, A., Lajoie, B.R., Dekker, J., and Mirny, L.A. (2012). Iterative correction of Hi-C data reveals hallmarks of chromosome organization. Nat Methods *9*, 999-1003. 10.1038/nmeth.2148.
124. Venev, S., Abdennur, N., Goloborodko, A., Flyamer, I., Fudenberg, G., Nuebler, J., Galitsyna, A., Akgol, B., Abraham, S., Kerpedjiev, P., and Imakaev, M. (2021). open2c/cooltools: v0.4.0 (v0.4.0). Zenodo. https://doi.org/10.5281/zenodo.4667696.

125. Hsieh, T.S., Cattoglio, C., Slobodyanyuk, E., Hansen, A.S., Rando, O.J., Tjian, R., and Darzacq, X. (2020). Resolving the 3D Landscape of Transcription-Linked Mammalian Chromatin Folding. Mol Cell *78*, 539-553 e538. 10.1016/j.molcel.2020.03.002.
126. Krietenstein, N., Abraham, S., Venev, S.V., Abdennur, N., Gibcus, J., Hsieh, T.S., Parsi, K.M., Yang, L., Maehr, R., Mirny, L.A., et al. (2020). Ultrastructural Details of Mammalian Chromosome Architecture. Mol Cell *78*, 554-565 e557. 10.1016/j.molcel.2020.03.003.
127. Li, H. (2021). New strategies to improve minimap2 alignment accuracy. Bioinformatics. 10.1093/bioinformatics/btab705.
128. Li, H. (2018). Minimap2: pairwise alignment for nucleotide sequences. Bioinformatics *34*, 3094-3100. 10.1093/bioinformatics/bty191.
129. Sarkans, U., Gostev, M., Athar, A., Behrangi, E., Melnichuk, O., Ali, A., Minguet, J., Rada, J.C., Snow, C., Tikhonov, A., et al. (2018). The BioStudies database-one stop shop for all data supporting a life sciences study. Nucleic Acids Res *46*, D1266-D1270. 10.1093/nar/gkx965.
130. Stirling, D.R., Swain-Bowden, M.J., Lucas, A.M., Carpenter, A.E., Cimini, B.A., and Goodman, A. (2021). CellProfiler 4: improvements in speed, utility and usability. BMC Bioinformatics *22*, 433. 10.1186/s12859-021-04344-9.
131. Eastman, P., and Pande, V. (2010). Openmm: A hardware-independent framework for molecular simulations. . Computing in Science & Engineering *12*, 34-39.
132. Nuebler, J., Fudenberg, G., Imakaev, M., Abdennur, N., and Mirny, L.A. (2018). Chromatin organization by an interplay of loop extrusion and compartmental segregation. Proc Natl Acad Sci U S A *115*, E6697-E6706. 10.1073/pnas.1717730115.
133. Davidson, I.F., Bauer, B., Goetz, D., Tang, W., Wutz, G., and Peters, J.M. (2019). DNA loop extrusion by human cohesin. Science *366*, 1338-1345. 10.1126/science.aaz3418.
134. Kim, Y., Shi, Z., Zhang, H., Finkelstein, I.J., and Yu, H. (2019). Human cohesin compacts DNA by loop extrusion. Science *366*, 1345-1349. 10.1126/science.aaz4475.
135. Golfier, S., Quail, T., Kimura, H., and Brugues, J. (2020). Cohesin and condensin extrude DNA loops in a cell cycle-dependent manner. Elife *9*. 10.7554/eLife.53885.
136. Tamm, M.V., Nazarov, L.I., Gavrilov, A.A., and Chertovich, A.V. (2015). Anomalous diffusion in fractal globules. Physical review letters, *114*, 178102.
137. Polovnikov, K.E., Gherardi, M., Cosentino-Lagomarsino, M., and Tamm, M.V. (2018). Fractal Folding and Medium Viscoelasticity Contribute Jointly to Chromosome Dynamics. Phys Rev Lett *120*, 088101. 10.1103/PhysRevLett.120.088101.

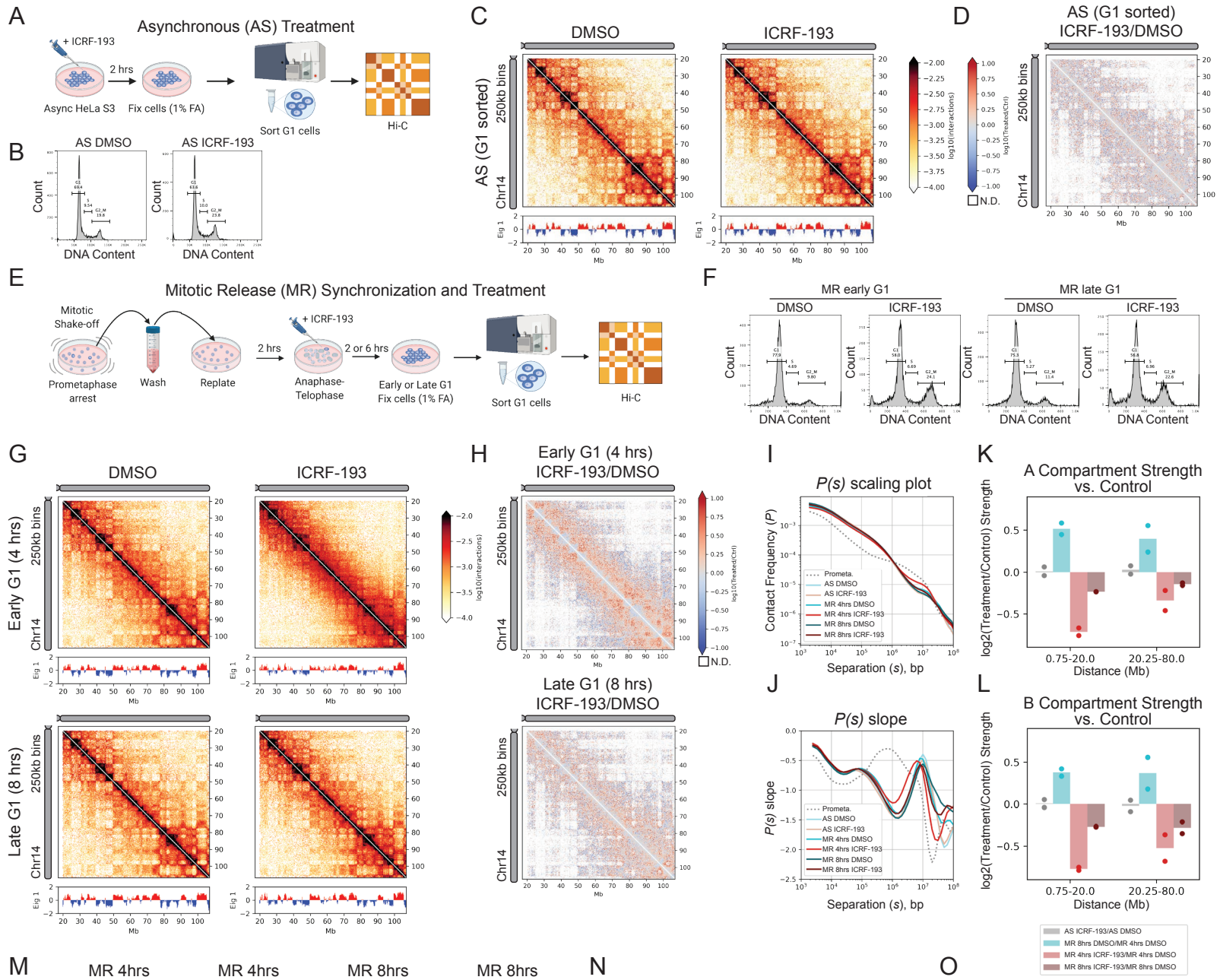


Figure 1: Topo II inhibition by ICRF-193 delays compartment re-establishment at G1 entry

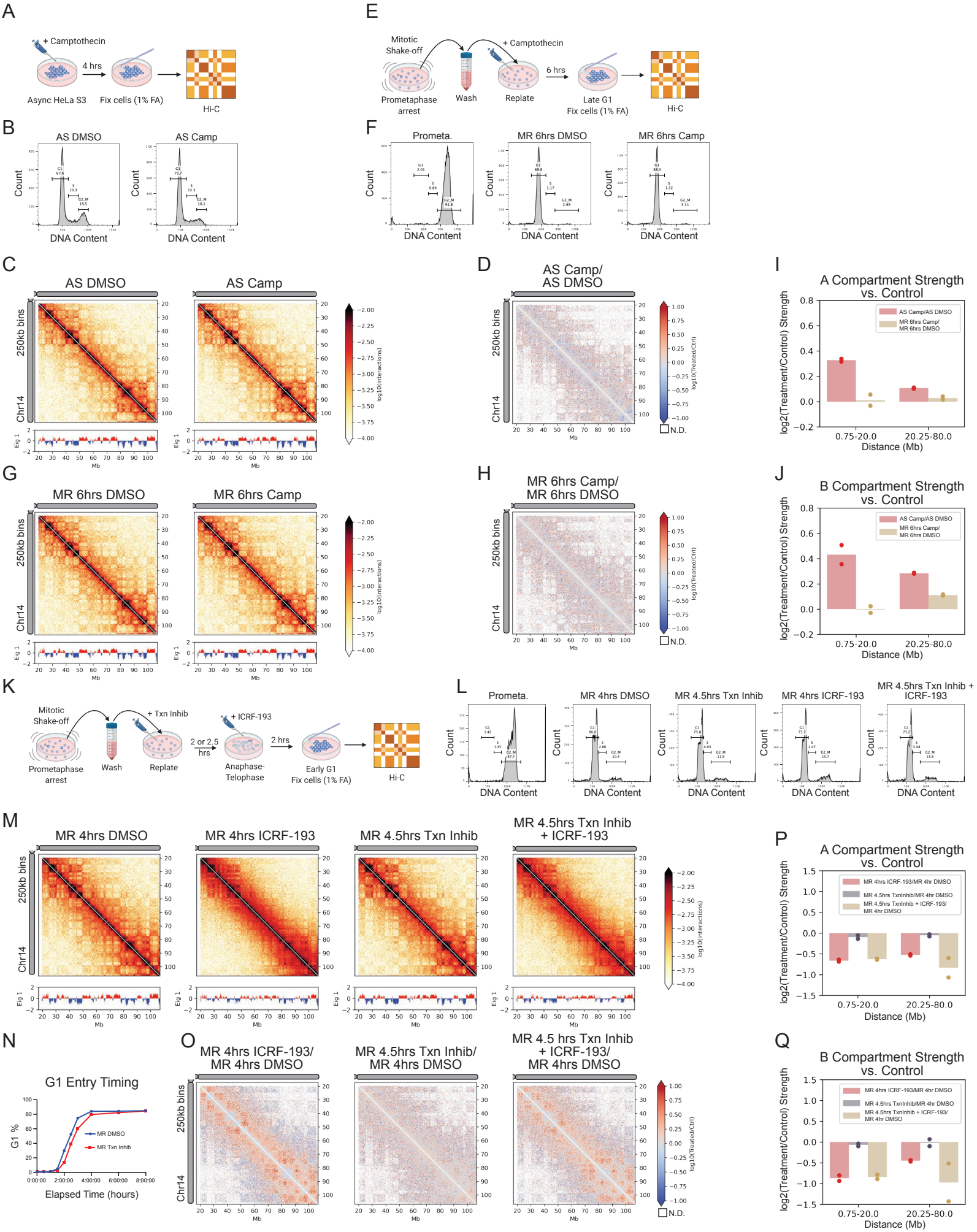


Figure 2: Changes in supercoiling and transcription do not phenocopy Topo II inhibition by ICRF-193

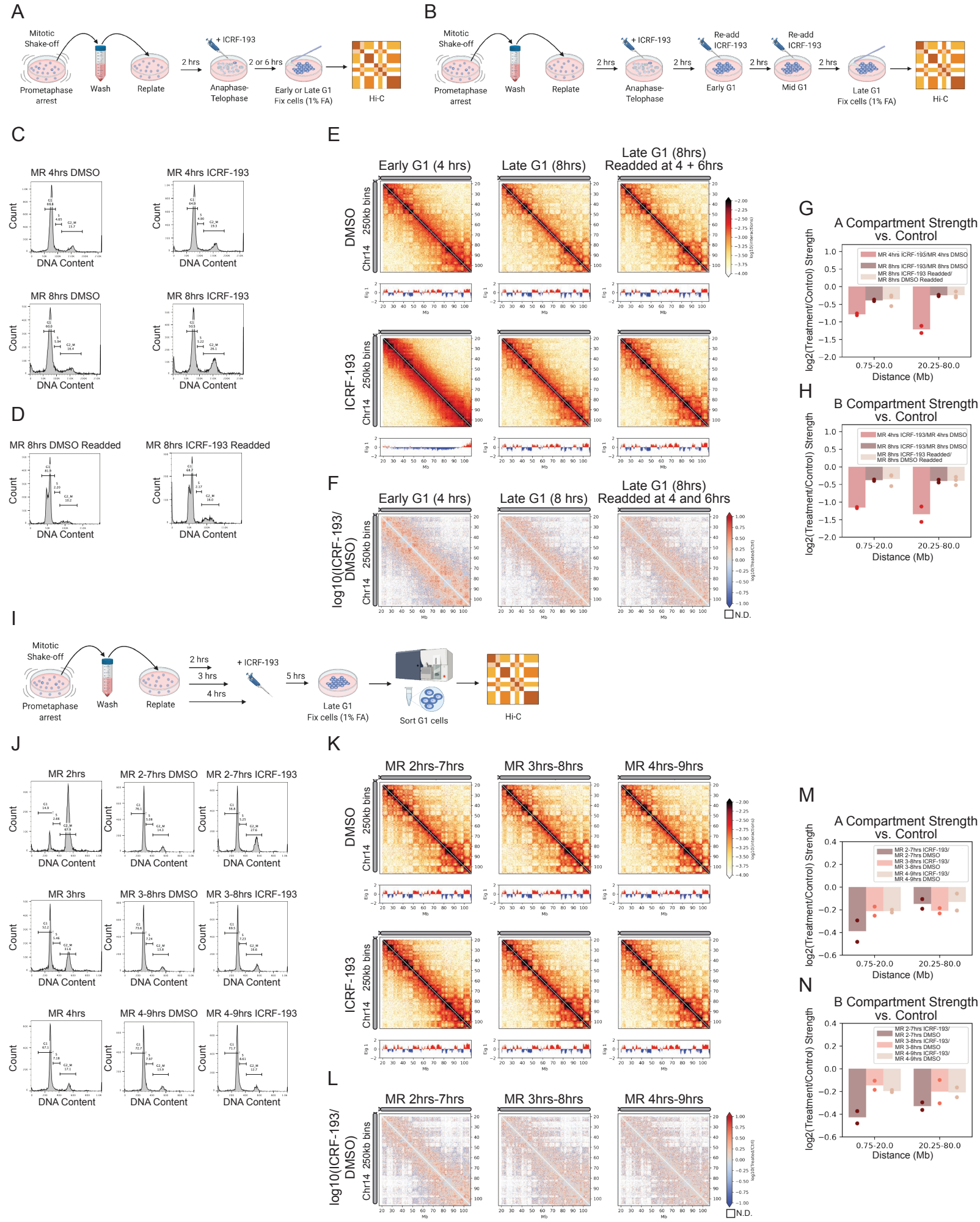


Figure 3: Topo II inhibition must occur during mitotic exit to delay compartment establishment

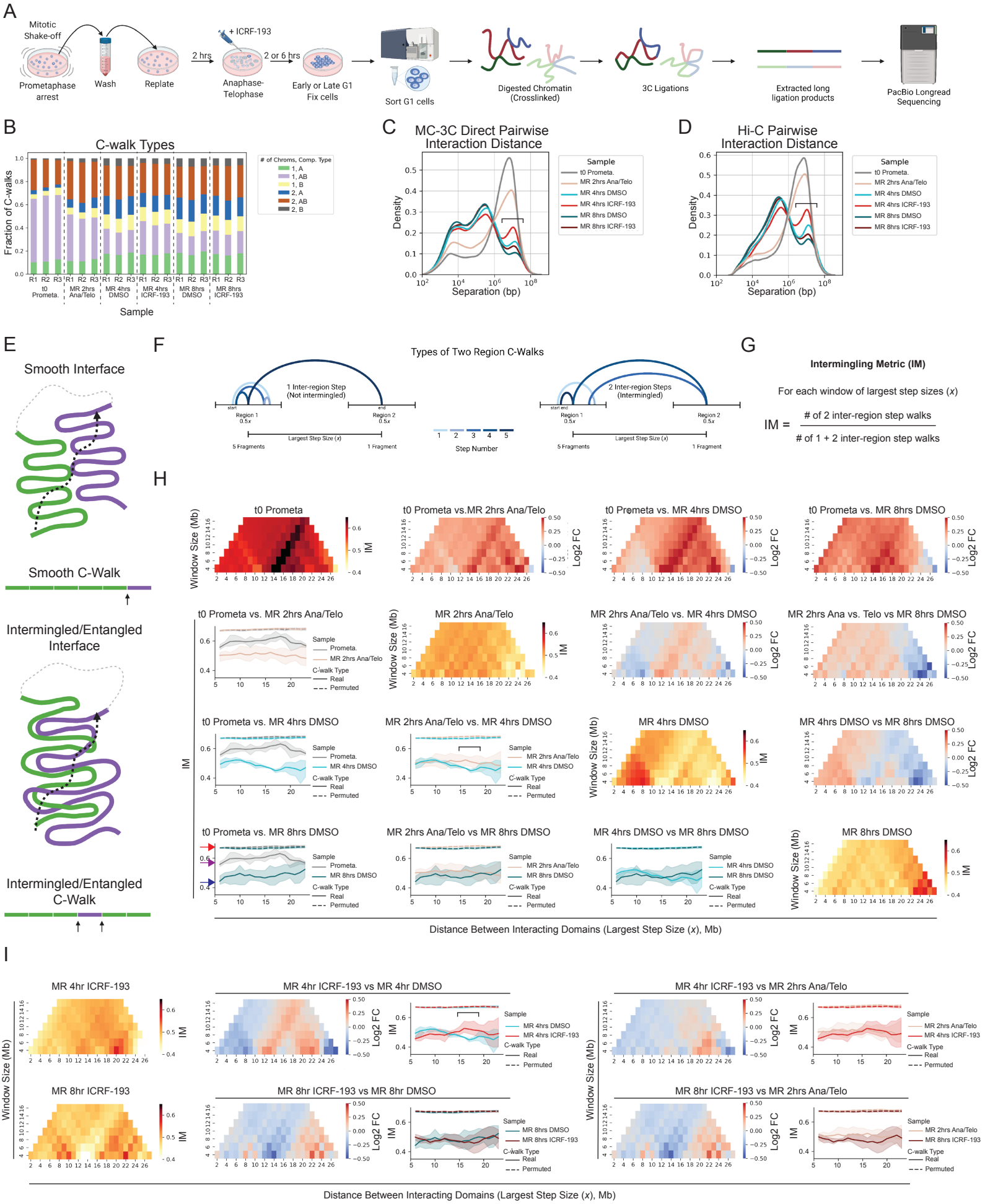


Figure 4: Topo II resolves mitotic entanglements during G1 establishment of interphase chromosome folding

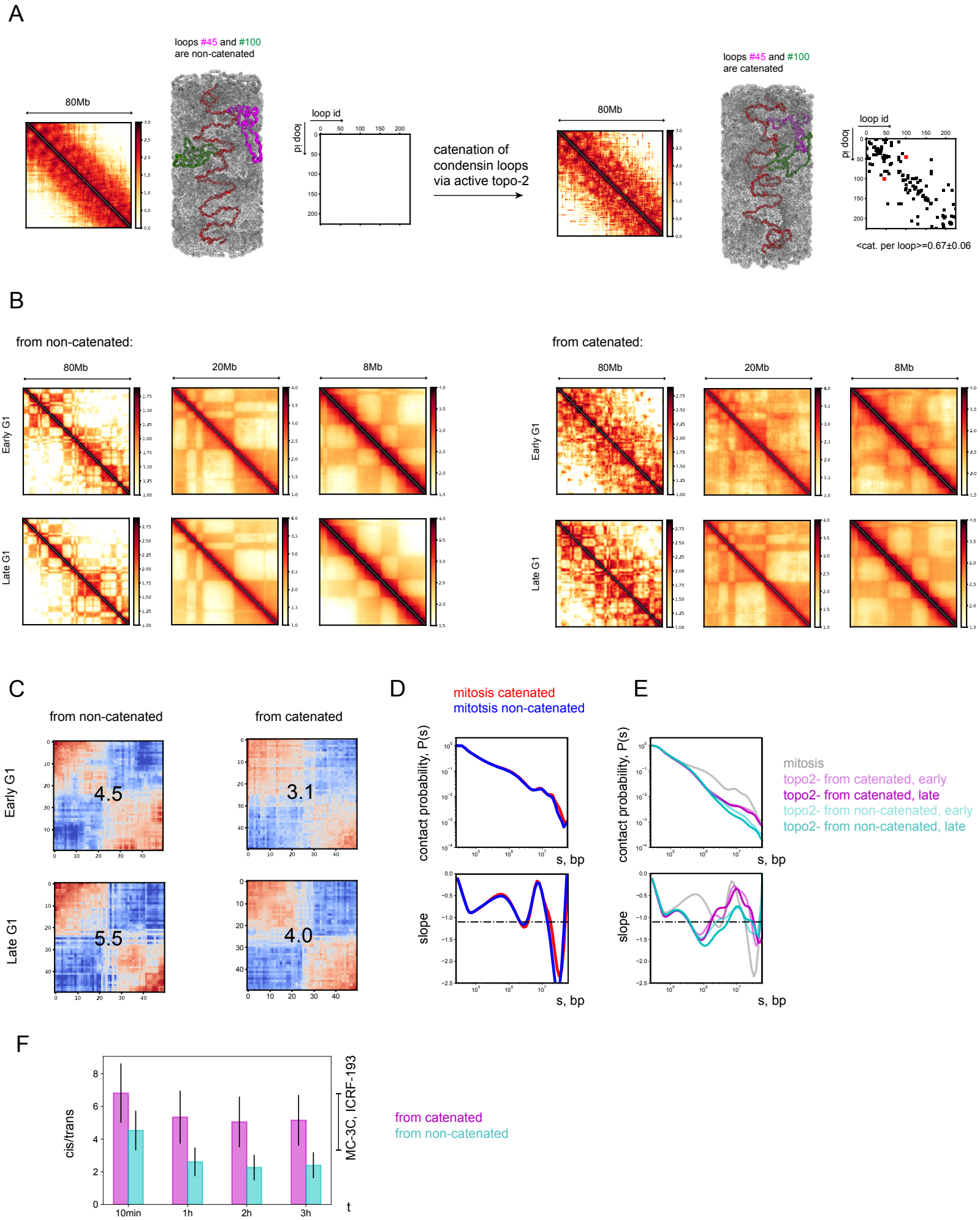
A
loops #45 and #100 are non-catenated
80Mb
loop id
catenation of condensin loops via active topo-2
loops #45 and #100 are catenated
<cat. per loop>=0.67±0.06
B
from non-catenated:
from catenated:
80Mb
20Mb
8Mb
Early G1
Late G1
C
from non-catenated
from catenated
4.5
3.1
5.5
4.0
D
mitosis catenated
mitotsis non-catenated
contact probability, P(s)
slope
s, bp
E
mitosis
topo2- from catenated, early
topo2- from catenated, late
topo2- from non-catenated, early
topo2- from non-catenated, late
F
cis/trans
MC-3C, ICRF-193
10min
1h
2h
3h
t
from catenated
from non-catenated

Figure 5

Instantaneous (one-stage) mitotic exit:

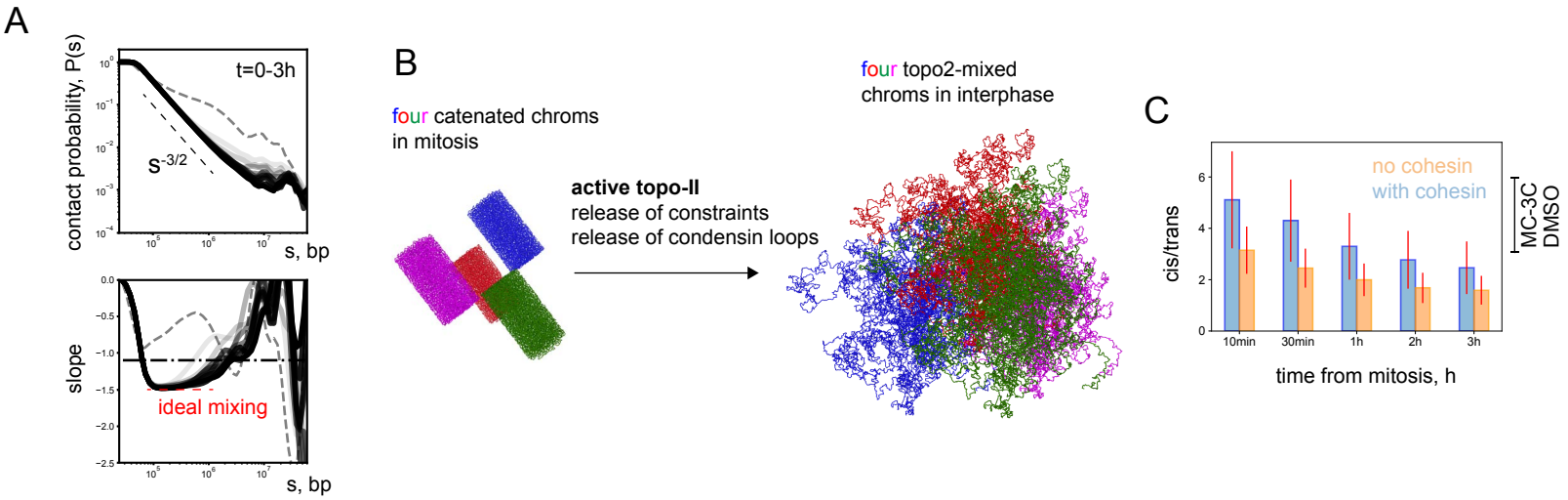


Two-stage exit:

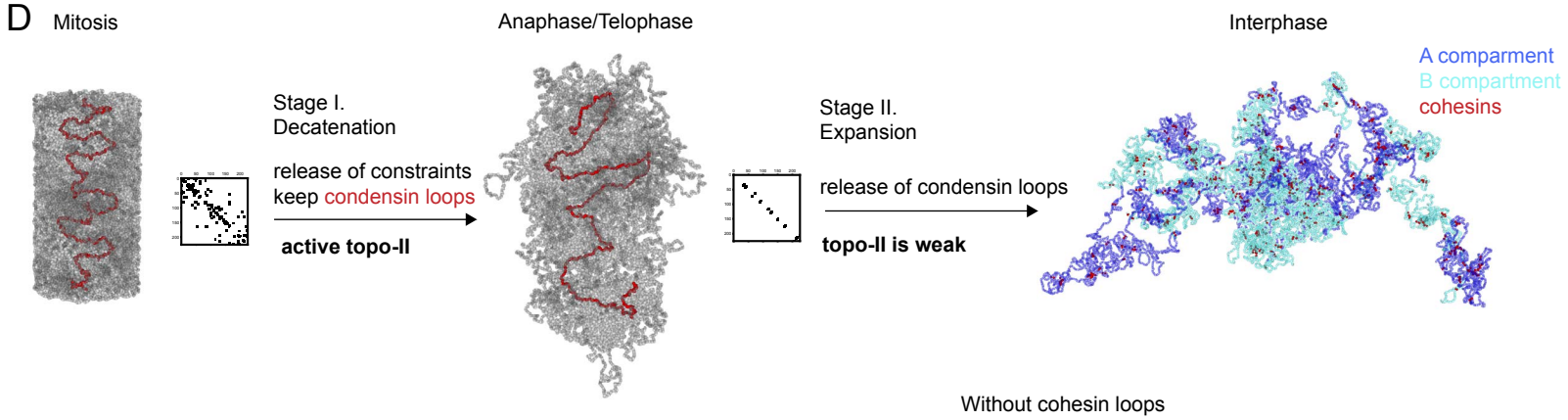


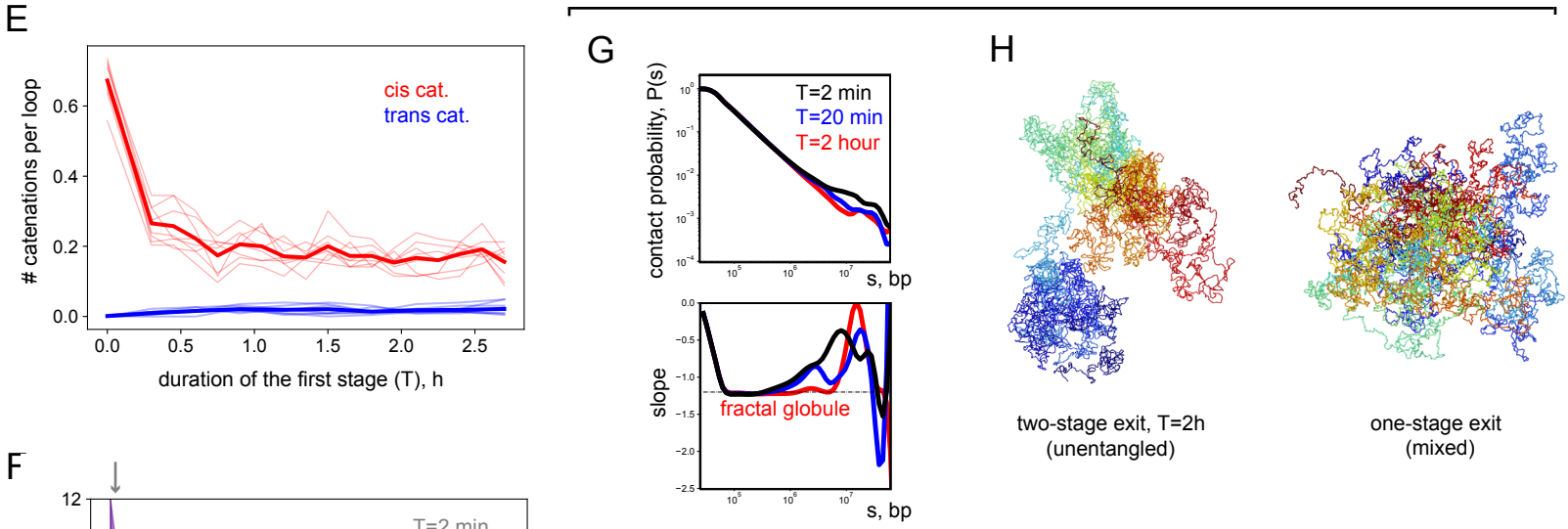


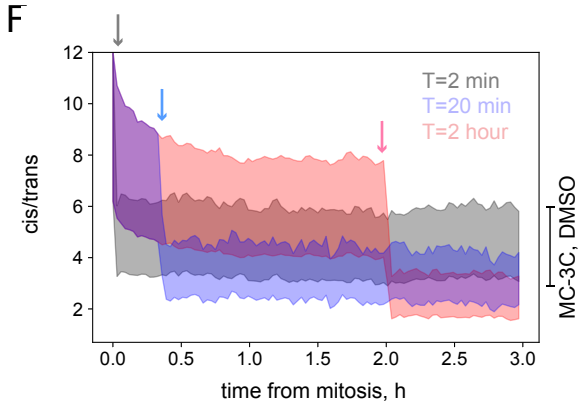


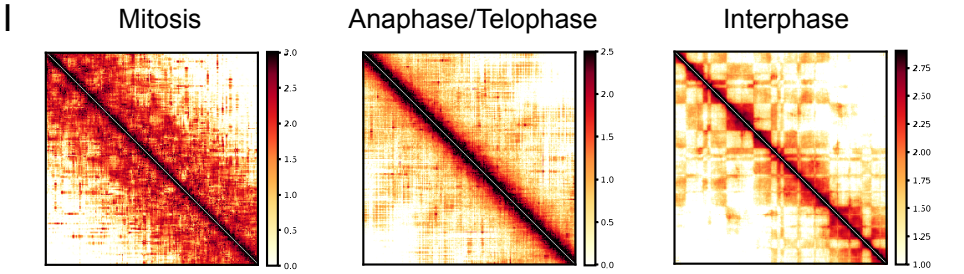


Figure 6

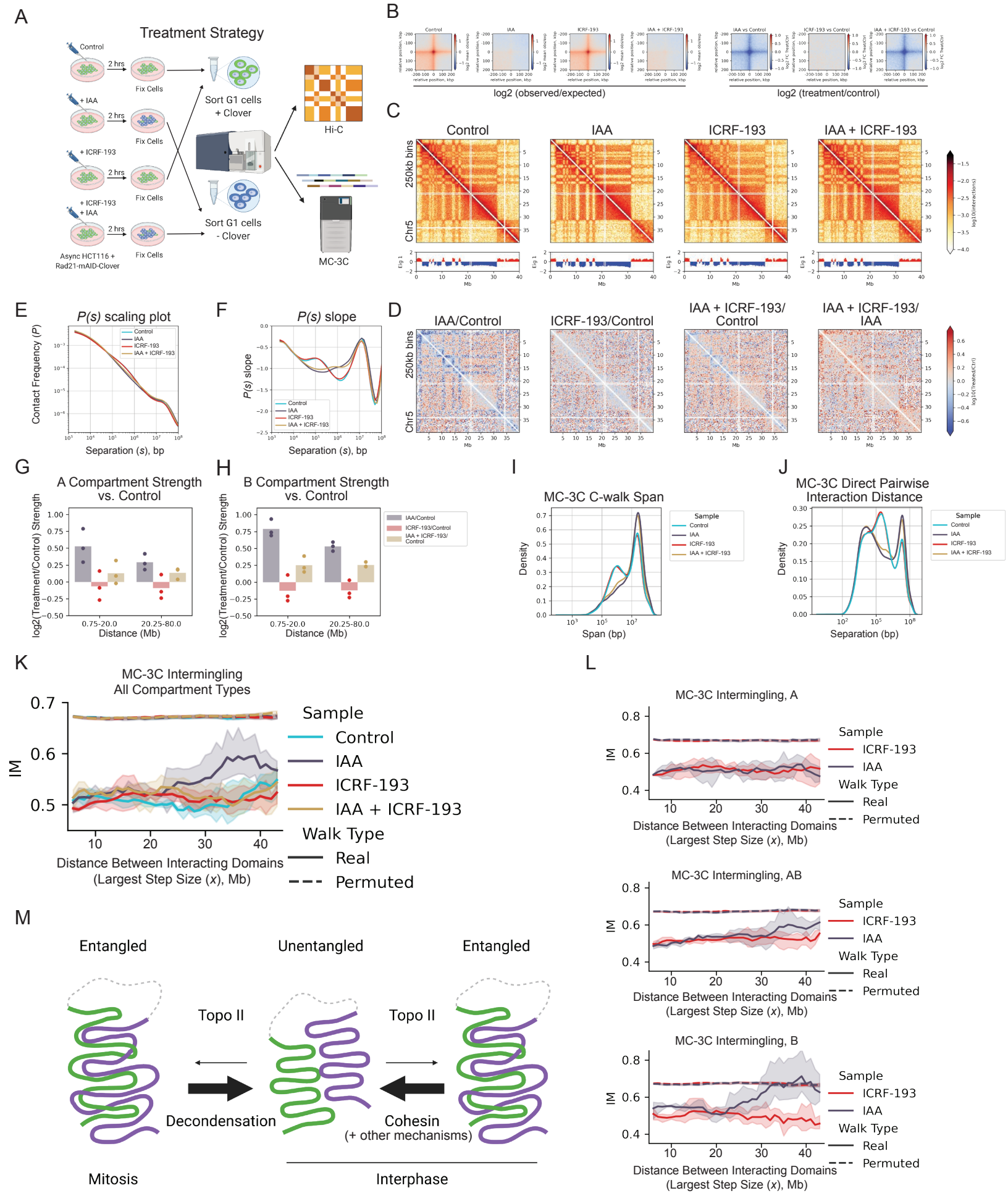


Figure 7: Cohesin directs Topo II activity to disentangle long-range compartment interactions